Atomistic Simulation Study of Star-shaped Polystyrene Melts

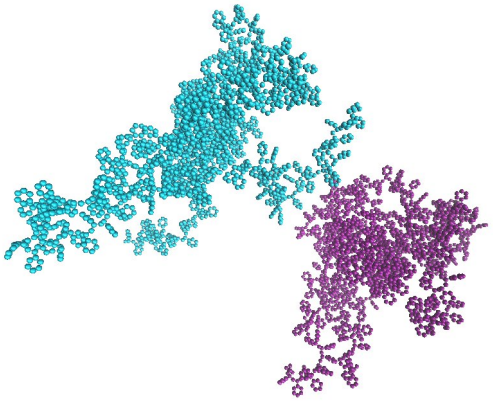

Eirini Gkolfi

Supervisors:

Dr. P.Bačová
Prof. V.Harmandaris

Thesis committee:

Prof. V.Harmandaris
Prof. S.Anastasiadis
Prof. S.Komineas

Master Thesis

Department of Mathematics and Applied Mathematics
University of Crete, Heraklion 2019

UNIVERSITY OF CRETE

FORTH
INSTITUTE OF APPLIED & COMPUTATIONAL MATHEMATICS

Acknowledgements

This thesis would not have been completed without the participation of so many people that I am more than thankful to. May not all of them will be mentioned namely but their contribution, in each way, was really essential and is gratefully acknowledged.

First of all, I would like to express my deepest gratitude personally to my supervisors. Primarily to Prof. Vangelis Harmandaris for giving me the opportunity to be involved in such an interesting project as well as his continuous support, knowledge-sharing, understanding and valuable guidance during all the period of my master studies. Furthermore I indebted like to thank Dr. Petra Bačová for sharing her knowledge, answering all my questions again and again, her endless patience and presence whenever I needed her, and most importantly for providing me with good basis for the area of research. It is really an honor to be guided from both of you! In addition, I would like to thank our ″experimental collaborators″ from FORTH, Dr. E.Glynos and Prof. S.Anastasiadis for a very fruitful collaboration.

Secondly, but not less importantly, I would like to express how greatfull I am to my family that supported me in every possible way. It is due to their support that I am at this point of my career today. I am also really thankful to all my friends who stand by me all this time and always try to encourage me as well as all the people whom I have shared ideas and problems with or helped me in any other way during this journey.

This work have not been possible without the financial support of the General Secretariat for Research and Technology (Action KRIPIS, project AENAO, MIS: 5002556).

Abstract

This work concerns a computational study of complex polymeric systems. We investigate the behavior of polystyrene (PS) star-shaped polymers with a variety of functionalities (number of arms) through atomistic molecular dynamic simulations. We simulate three types of systems, namely a) PS stars in melts, b) PS stars in blends with linear chains and c) PS stars in melts with modifications of the internal structure.

Our atomistic model captures chemical characteristics of polystyrene, allowing us to obtain quantitative information about the structural properties of the material that is not easily accessible by experiments or coarse-grained simulation models. We perform extensive equilibration and production runs in order to be able to compute a range of statistical quantities.

The analysis focuses on the intramolecular structure and the morphology of the material. The results are analyzed as a function of the star functionality. The obtained conformational characteristics are compared with well-known theoretical models. A comparison of the properties of stars in two external environments, i.e., in melt and in a blend with linear chains is also made. Additionally, we study quantitatively the internal impenetrable region of the stars via a novel geometric algorithm. The impenetrable region is also present in the systems such as soft colloids or hairy particles and is responsible for a complex dynamical behavior of the material.

The aim of our study is to bridge the gap between the theoretical models and the experimentally observed phenomena of star-shaped polymers by providing an insight into the morphology of polystyrene stars at nanoscale.

Contents

1. Introduction

1.1 Polymer materials

In our every-day life we come into contact with plenty of materials. The majority of them are polymer products. Polymers are divided into natural and synthetic. Natural polymers, also called biopolymers, are produced by living systems. Some examples of them are proteins in the human body, DNA and polymers from trees such as natural rubber. We are all familiar with synthetic polymers as we can find them in many well-used products such as tires, nylon, stockings, resins etc. Over time synthetic polymers have become the best, or indeed only, choice for a wide variety of applications [1]. Even materials as glass, wood and iron were massively replaced by different types of polymers with similar physical properties as the substituted materials.

Although some of the first synthetic polymers were discovered during the nineteenth century, the first polymer materials were manufactured and used around 1930. One reason for that was the need, in the inter-war years, to find replacements for natural polymers, such as rubber for financial reasons. A second reason was that there was by then an understanding of the nature of these materials. In 1910, Pickles had suggested that rubber was made up of long chain molecules and after a number of studies, in 1926, Staudinger developed the idea which became accepted by the scientific community [1]. It is worth mentioning that the very first polymeric syntheses were those of cellulose in 1846 and of Bakelite in 1907. However, it took 30 years for cellulose to be used as a synthetic material. During the war in 1914-1918, its derivative was used as a fire-proof dope for treating aircraft wings, later it contributed to improve an artificial silk and after some years of development it became the most important injection-moulding material. Cellulose is used till today in the manufacture of filter tips for cigarettes and in packaging materials. After the first commercial manufactures of a variety of polymeric types during the 1930s, many more types of polymers have been produced in order to improve the quality and the properties of the invented materials such as stiffness and heat resistance. As our needs change during the ages and every invention leads to new ideas for

improvements, different types of polymers are produced in laboratories all the time.

The word ″poly-mer″ derives from the Greek word ″πολυ-μερές″ which means ″many-parts″. As chemical entity a polymer is a complex substance consisting of smaller and simpler chemical repeated units (parts). These repeated units are called *monomers* and are attached to each other via covalent bonds in order to construct a polymeric chain. In general, a monomer can be an atom or just a small molecule composed of atoms. In this work we refer to monomers as a group of bonded atomic units (See Chap. 3). Polymers that contain monomers of only one type are called *homopolymers* while in any other case they are called *heteropolymers*.

The structure of a polymeric chain is generated during *polymerization*, the process by which elementary units (monomers) are covalently bonded together [2]. The number of the contributed monomers n is called *degree of polymerization*. In Fig. 1.1 we present a scheme of the polymerization of styrene monomers generating the polymer called polystyrene (PS).

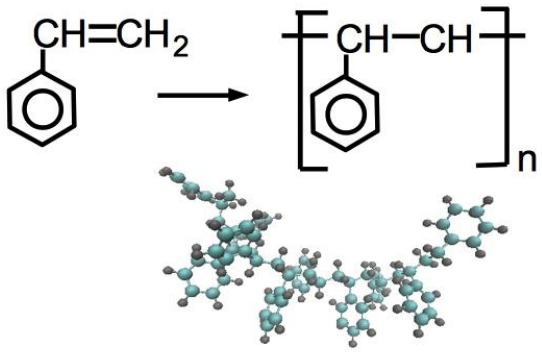

Figure 1.1: Process of polymerization of styrene monomer in order to produce polystyrene (top) and a snapshot of a model polystyrene chain (down). n denotes the number of the attached monomers (degree of polymerization).

The major factors that affect the properties of a polymeric system and consequently of the corresponding polymer material are the chemical identity of the monomers, their number along the macromolecular chain (degree of polymerization) and the monomeric structure of the atoms along the chain. Once the double bond of the monomer breaks, during this process, a variety of different isomers are possible for the repeating units along the chain [2]. The term isomer is used for the molecules with identical formulas but distinct structures. However, isomers do not necessarily share similar properties [3]. In Fig. 1.2 we present an example of a type of stereoisomerism that is described by polymer's tacticity. Assume a macromolecular chain with a backbone of carbon atoms

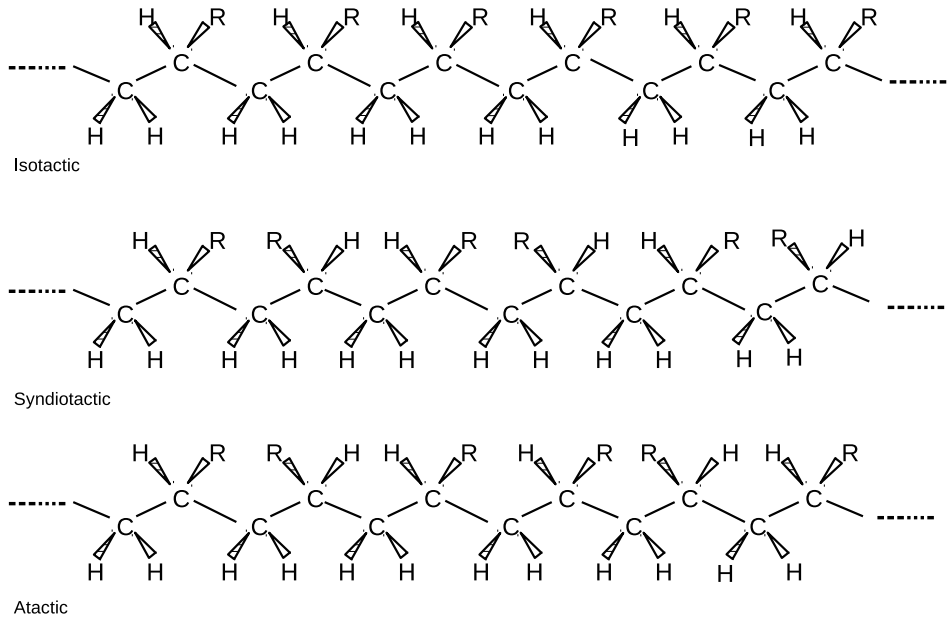

Figure 1.2: Representation of polymers tacticity: Isotactic, syndiotactic and atactic.

and as ″side-groups″ hydrogen and an arbitrary R group every second carbon. The four single bonds, emanating from a carbon atom, have a sp3 hybridization structure. Sp3 structure, geometrically, means that the four bonds form a tetrahedral with an angle of 109 ° between them and the central C atom.

If all backbone carbon atoms of a polymer are arranged in a zig-zag conformation along the same plane, adjacent monomers have either their R group on the same or different sides of this plane. If all the R groups of a polymer are on the same side of the chain, the polymer is isotactic. If the R groups alternate regularly, the polymer is syndiotactic and if their placement is completely random the polymer is atactic [2] (see Fig.1.2).

Apart from the linear chain, that is actually the polymeric chain without any branching events, there are polymers with much more complex architecture that are composed of linear chains attached together into a given structure. The differences in architecture of a polymer lead to different dynamics and consequently to different properties. Some examples are: the ring that is a linear polymer with its ends attached, star-shaped, branched and the network-

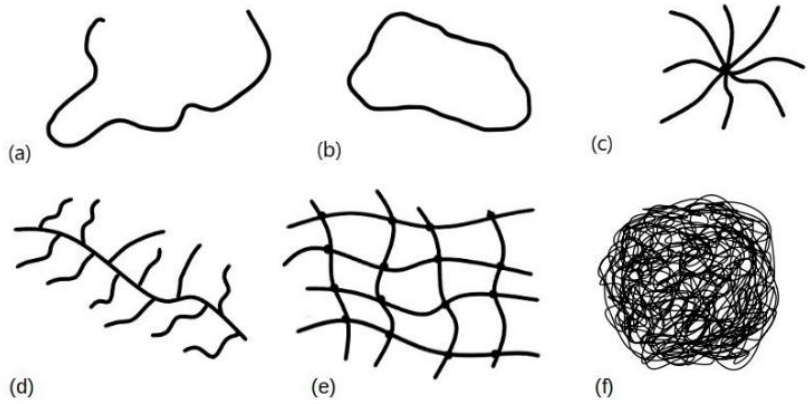

Figure 1.3: Examples of polymer architectures: (a) linear, (b) ring, (c) star-shaped, (d) branched, (e) network and (f) colloid.

like structure as they are presented in Fig. 1.3.

A star polymer is composed of linear chains attached to a common branch point. The number of attached linear chains (arms) is called functionality f of the star. Star polymers are gaining interest because of their compactness and enhanced segmental density as compared to their linear polymers of the same molecular weight.

This star-like polymer kind of architecture can be described as intermediate between the two extremes in a spatial organization of a large number of low molecular units: (a) linear, flexible polymeric chains and (b) hard colloidal particles. Colloids are stiff compact assemblies with a predominantly spherical shape. Both linear polymer and colloids are widely studied and used in a variety of applications, as they exhibit very interesting properties [4]. The intermediate behavior between short-range linear polymers and long-range colloidal interactions is a rich area of research because of the great potential to combine polymers with colloidal mesoscopic characteristics. A way of studying this behavior is by constructing more complex architectures that combine characteristics of them both, like star-shaped polymers. For this reason star-polymers have been studied extensively in recent years via various experimental techniques [5, 6, 7, 8, 9].

According to Daoud and Cotton [10] stars with high number of arms exhibit a nonuniform monomer density profile. The density of arm segments is the highest in the central core region and decreases towards the end of the arms where the chain segments have the largest configurational freedom [10, 11]. An important quantity is the penetrability of the stars, which shows how easily a

star polymer can be penetrated by neighboring elements. For a large number of arms (increasing functionality), star-shaped polymers resemble more closely the ″hard sphere″ model than linear chains behavior, they become less penetrable and exhibit liquid-like behavior. According to Pakula [12] the functionality above which the stars do not completely penetrate each other in a melt system is $f > 24$ and there is a central core in each star which remains not accessible from elements of neighboring molecules. Such materials with intermediate properties are expected to present rich dynamics in contrast to the simpler behavior of the two extremes [4].

The complex interplay of dynamical processes affects an important property of polymers called viscoelasticity. Viscosity of a fluid is a measure of its resistance to deformation at a given rate but in liquids, it corresponds to the informal concept of friction. Elasticity is the ability of a body to resist a distorting influence and to return to its original size and shape when that influence or force is removed. For polymers, elasticity is caused by the stretching of polymeric chains when forces are applied. Polymers are viscoelastic and exhibit some of the properties of both viscous liquids and elastic solids. The viscoelastic response of a polymer depends on many factors, such as temperature, the rate at which the polymer is deformed, its internal structure etc.

In the current work, we investigate melt systems of atactic star-shaped polystyrene (PS) polymers. A melt system refers to a highly dense system without solvent. In our case all the arms of the star are identical (homopolymer-arm stars). In polystyrene (See Fig. 1.1), the polymerized monomer, styrene, is a derivative of petroleum and it is a vinyl monomer of type CH2=CHR. R stands for an aromatic ring (C_6H_5) which is a cyclic, planar compound. As this monomer is composed only of carbon (C) and hydrogen (H) atoms it is called aromatic hydrocarbon.

Polystyrene is a versatile material used to make a wide variety of consumer products both in solid and foam forms. As a hard, solid material, it is often used in products that require transparency, such as food packaging and laboratory ware. When combined with various colorants, additives or other polymers, polystyrene is used to make appliances, electronics, automobile parts, toys etc. Foam polystyrene can be more than 95 percent air and is widely used to make home and appliance insulation, lightweight protective packaging, surfboards, roadway and roadbank stabilization systems etc. Lightweight polystyrene foam provides excellent thermal insulation in numerous applications, such as building walls and roofing, refrigerators and freezers, and industrial cold storage facilities. Polystyrene insulation is inert, durable and resistant to water damage. Styrene also occurs naturally in foods such as strawberries, cinnamon, coffee and beef [13].

1.2 Modelling of polymer materials

The beginning of the computer simulations comes in the early 1950s when electronic computers became partly available for nonmilitary use. Before, computer simulation started as a tool to exploit the electronic computing machines that had been developed during and after Second Word War which performed heavy computations involved in nuclear weapons and code breaking [14].

In very simple words, computer simulation is a program, running on the computer, which imitates a real-life system and is able to explore the approximate behavior of a mathematical model [15, 16]. This system can be biological, physical, financial, even sociological. The program is actually an algorithm that takes as input an initial state of the system at given conditions and as an output gives its final state. The new states are given by solving numerically the equations that describe the mathematical model of the system under investigation. The degree of difficulty of this process depends on the complexity of the corresponding equations.

The basic laws of nature as we know them are expressed in terms of equations which we cannot solve exactly and this is why the computer simulation method is so important. For example, for the motion of more than two interacting bodies, even the relatively simple laws of Newtonian mechanics become hardly analytically solvable as the trajectories become deterministic chaotic [17, 14]. In such cases of models described by differential equations, the computer simulation methods are not only the best option but also the only one for the prediction of the system's evolution. Polymeric systems, as they are composed of many interacting ″bodies″ whose motion is described by differential Newton's equations, constitute such a case. Their evolution in time is studied through molecular dynamic (MD) simulations.

Before the appearance of computer simulation the only way to predict the properties of a molecular substance was by using a theory that provided an approximate description of that material. The problem was that there are very few systems for which the equilibrium properties can be computed exactly from the theory so the most properties of real materials were predicted on the basis of approximate theories [14]. Even by trying to take into account the intermolecular interactions the problem cannot be solved as our knowledge of them is limited. Furthermore, if the experimental data disagree with the predictions, it means that our theory or our estimation of the intermolecular interactions, or even both, are not accurate. This is where the computer simulations come to bridge the gap between the analytical theory and the experiments. Through simulations, if the results disagree with the experiments, we can improve our model while if they disagree with the theory, we know that our theory is flawed. Comparing to the experiments, simulations have also some advantages such as

the lower cost and the easier human intervention like pausing and restarting the process.

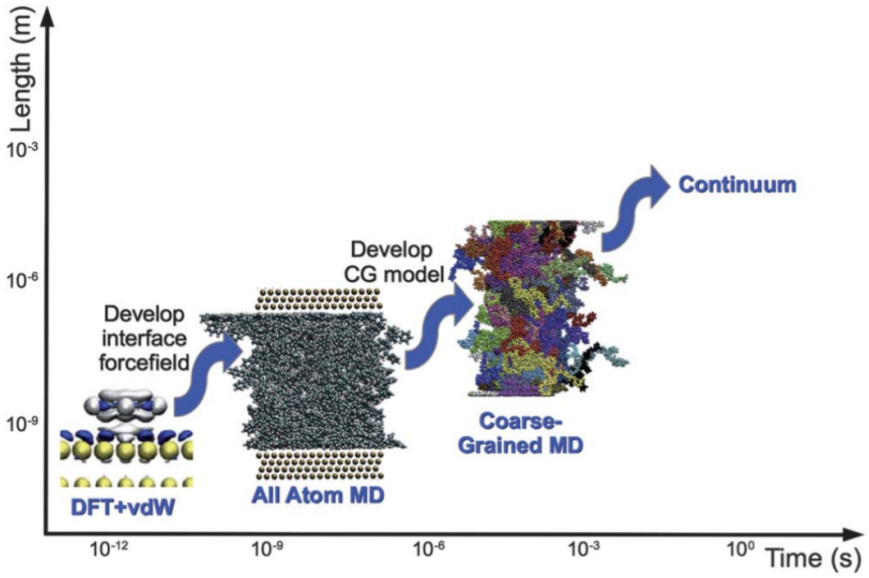

Figure 1.4: Multiscale modelling of polymer–solid interfaces from the electronic structure level, through the atomistic level, to the mesoscopic coarse-grained level and beyond taken from Ref. [18].

Simulations of macromolecules are very challenging because of the wide range of time and length scales involved since there are different characteristic time scales associated with the motion of various segments of the polymeric chain [18]. Although during the experiments we can investigate the interactions in different length scales along the examined area, during simulation it is difficult to treat the broad range of time and length scales simultaneously. Thus, we use different approaches to model them in various levels of description.

The standard approach in material science is to average out the details at the molecular level and simulate at continuum level using, for example, fluid dynamics or finite element methods. This relies on input parameters that describe natural properties, such as viscosity and density, which are usually assumed to be constant throughout the model system and not always known. Also, this approximation breaks down at nanoscale level [18]. For a more detailed description, there are two particle-based simulation methods divided into coarse-grained (CG) and atomistic. Both of them have been used to predict structural and dynamical properties at molecular level. A coarse-grained model represents groups of atoms by a single particle, used to describe systems in mesoscopic regimes. The choice of the CG representation is very important for

every CG approach and depends on the physical problem and the questions to be addressed. An atomistic model is a detailed all-atom presentation of the system and provides more quantitative comparison between realistic model systems and experimental quantities. The accuracy of atomistic models depends on the classical force fields, which are usually not designed to describe changes in chemical bonding. To understand chemical bonding we use quantum mechanical methods [18]. Fig. 1.4, taken from Ref. [18], is a typical length-time representation that describes hierarchical multiscale simulation methodologies.

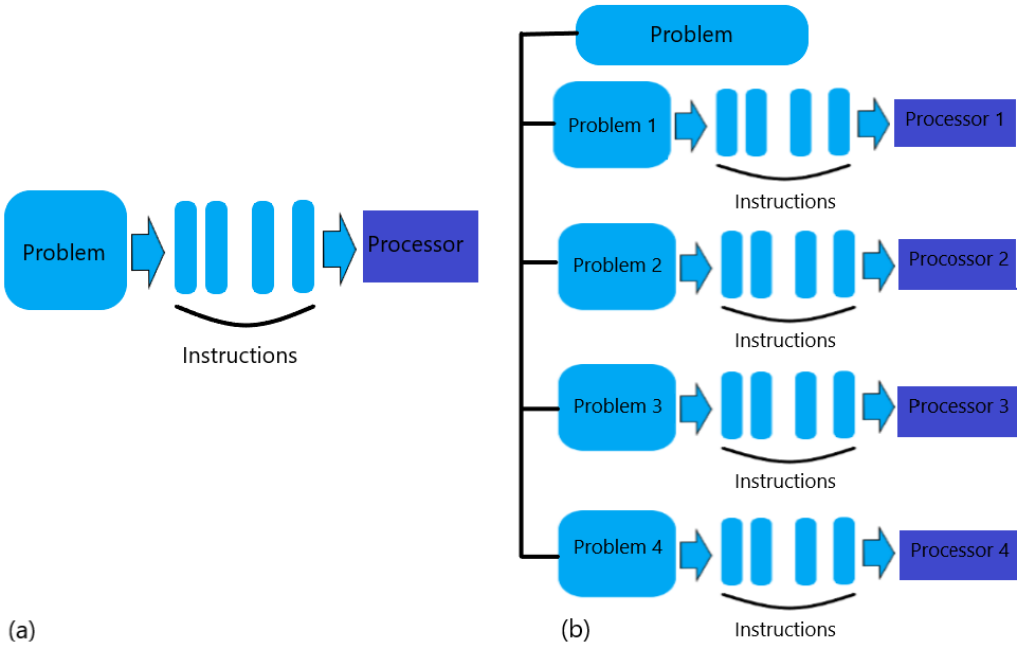

Figure 1.5: (a) Serial computing where the problem is divided into instructions that are executed one-by-one in one processor (b) Parallel computing where the problem is divided into subproblems. Each one is executed in different processors at the same time.

In the current work we perform atomistic molecular dynamics simulations. Atomistic simulations of complex macromolecules result in a big number of the ″interacting bodies″ in our system. This means that for simulating such real-life's systems we need a huge number of calculations and equations to be solved, which in the computer language refers to high computational cost. To overcome this problem the parallel programming has been introduced.

In traditional, serial, computations the problem is broken into a discrete series of instructions that are executed sequentially one after another on a single processor, which means that only one instruction may execute at any moment

in time. Parallel programming is the division of a problem into smaller ones. Each subproblem is further broken down to a serie of instructions while the instructions from each part execute simultaneously on different processors [19]. In Fig. 1.5 we present both processes.

To achieve efficient parallel computation, the problem should have some features. First of all, it should be able to be broken into discrete pieces of work that can be solved simultaneously. Consequently, it has to be capable of executing multiple program instructions at any moment in time and -as we use parallel programming in order to save time- we should make sure that the problem will be solved in less time with multiple compute resources than with a single compute resource [19]. There are two compute resources which we can use for parallel programming: either a single computer with multiple processors/cores, or a computer cluster consist of an arbitrary number of such computers connected by a network. Each computer of the network is referred as 'node' and in this way larger parallel computer clusters are made.

1.3 Challenges addressed in this thesis

The aim of this work is to perform atomistic simulations of star-shaped PS polymers of a variety of functionalities ($f = 4, 8, 16, 32$) in two types of systems (melts and blends) and with two types of internal structure.

The big challenge is that, to our knowledge, star-like polymers in melt have not been studied before by an atomistic model. There are studies only for bead-spring models (CG). Recently, atomistic simulations of mikto-arm stars in vacuum and in blends with short linear polymers have been published by members of our group [20, 21]. One of the difficulties of atomistic simulations is the high number of computations as more atomic units than in CG models are involved in order to model a specific system. To achieve good statistics for the estimation of quantities of interest, we need multiple molecules in each system. This leads to very time-consuming simulations as the number of numerical operations scales with N^2 for N representing the number of all the atoms in the system. In addition, because of the high density of melt systems and reduced mobility of the stars due to the branch-point presence, equilibration is very slow. We also face many problems while preparing the complex polymer architectures. However, atomistic simulations are much more precise and closer to reality as they take into account the specific chemistry of a given system, here polystyrene. They allow us to get a quantitative picture about the effect of functionality on the structural properties of the studied polymer material.

Many experimental studies deal with stars with long arms (more than 10 times longer than those in our study) [8, 22]). Recent experimental study of

PS stars with short arms (lengths comparable to our study) [11] showed that the functionality above which PS stars start to be hardly penetrable is $f > 8$. However, by using a general polymer model, Pakula [12] *et al.* estimated this transition to be around $f > 24$.

Having in mind the limitations of CG models and since during the experiments we are not able to look closely into nano (atomic) scales, the motivation for the current study is to bridge the gap between the theories and experiments and to get additional information about the structural properties of the PS stars.

2. Method

2.1 Molecular dynamics

Molecular Dynamics (MD) is a computer simulation method that is used to study the evolution of a molecular system [14]. In simple words, it is a way to imitate a real life's system, knowing in every step the positions and velocities of all the bodies it is composed of, its energy, density and a variety of other quantities of interest that we will discuss below.

This method gives us the opportunity to repeat the process as many times as we need -with the same or different initial conditions- or stop it and restart it again with a much lower cost than in real experiments. Moreover, we have better control over the conditions in simulations such as the temperature and the material composition than we have during a real-life experiment in a laboratory.

The simulated system consists of N atoms and/or molecules that interact with each other by the terms of a force field, or so-called interatomic potential. The problem of finding the positions and velocities of each one of them is called **N-body problem**. Thus, from now on, N will be the total number of the atoms composing the simulated system.

In order to estimate the quantities of interest in a simulation, we need to know the trajectory of the atoms in the system. The trajectory is determined by the positions and velocities (or momenta) in every step of the simulation. This information can be obtained by solving numerically the classical equations of motion of every molecule or atom in the system concerning all the interactions between them.

2.1.1 The MD algorithm

The procedure that we follow to export the trajectory and the quantities of interest in a simulation is very similar to the one that we follow in real life experiments. In a laboratory we first prepare the sample of the material we want to study under the corresponding conditions. Then, we connect the systems with the instruments to measure the quantities of our interest. During

the experiment we measure these quantities in specific time intervals in order to get statistical averages of them.

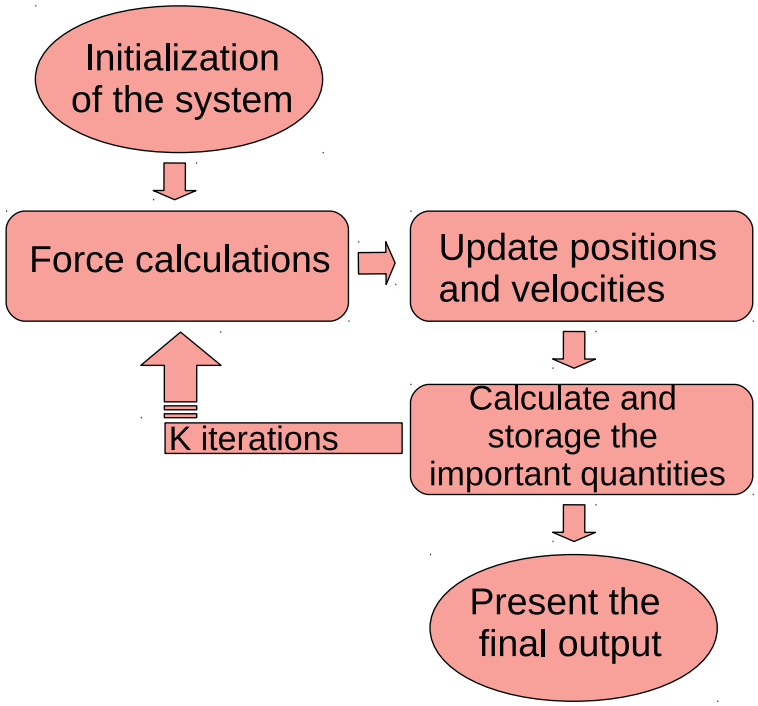

Figure 2.1: Graphical representation of the MD algorithm.

The corresponding protocol in computer simulations is very general and almost the same for all types of MD simulations. It is the so-called MD algorithm and its general scheme consists of the following steps:

1. We create the initial configuration of the system that consists of the initial positions and velocities for every particle and use it as an input of the algorithm.

2. We calculate the forces acting on every particle of the system.

3. We choose a numerical method to integrate the classical equations of motion in order to get the new positions and velocities, store them and replace the initial ones.

4. We calculate and store important quantities such as energy and density by using current positions and velocities.

5. Presentation of final output values.

The graphical representation of the algorithm is shown in Figure 2.1.

At step 1, for initializing the velocities one typical option is to generate them from a Maxwell-Boltzmann distribution given by:

$$P(v) = \left(\frac{m}{2\pi k_B T}\right)^{\frac{3}{2}} e^{\frac{-mv^2}{2k_B T}} \tag{2.1}$$

where v is the velocity of the corresponding particle, m stands for its mass, k_B is the Boltzmann's constant and T the actual temperature of the system.

During the MD simulation steps 2-4 are repeated as many times as it is necessary (let us say K). The integer K depends on the system's nature and properties which we want to investigate. The initial configuration and the corresponding conditions that actually specify the kind of the run (procedure) are adjusted according to the specific problem under study.

2.1.2 Equations of motion

In order to update positions and velocities in every time step in a system consisting of N atoms, we need to solve the equations of motion. If we denote as q_k the generalized coordinates describing the molecular configuration and $\dot{q}_k$ their time derivatives $\forall\ k = 1, 2, 3, ..., 3N$, in Lagragian formalism, the trajectory $\mathbf{q}(t)$=$(q_1(t), q_2(t), ..., q_k(t), ..., q_{3N}(t))$ satisfies the following differential equations:

$$\frac{\partial L}{\partial q_k} = \frac{d}{dt}\left(\frac{\partial L}{\partial \dot{q}_k}\right) \tag{2.2}$$

where L is the Langragian of the system and equals to $L(\mathbf{q}, \dot{\mathbf{q}}, t) = K(\dot{\mathbf{q}}(t)) - V(\mathbf{q}(t))$ while K represents the kinetic energy of the system and V its potential energy. The corresponding generalized momenta p_k is defined as:

$$p_k = \frac{\partial L}{\partial \dot{q}_k} \tag{2.3}$$

On the other hand, in Hamiltonian formalism, the generalized coordinates obey the Hamilton's equations:

$$\dot{q}_k = \frac{\partial H}{\partial p_k}, \qquad \dot{p}_k = -\frac{\partial H}{\partial q_k} \tag{2.4}$$

where the Hamiltonian is defined as:

$$H(\mathbf{p}, \mathbf{q}) = \sum_k \dot{q}_k p_k - L \tag{2.5}$$

In the case of independent of velocities and a constant (time independent) V, the Hamiltonian corresponds to the total energy of the system:

$$H(\mathbf{p}, \mathbf{q}) = K(\mathbf{p}) + V(\mathbf{q}) \tag{2.6}$$

In Cartesian coordinates, where the kinetic energy equals to $K(\dot{\mathbf{r}}) = \frac{1}{2}m\dot{\mathbf{r}}^2$ and the potential energy is denoted by $V(\mathbf{r})$, the Hamilton's equations 2.4, for $i = 1, 2, ..., N$, through 2.6 become:

$$\dot{\mathbf{r}}_i = \frac{\mathbf{p}_i}{m_i} = \mathbf{v}_i \qquad \dot{\mathbf{p}}_i = -\nabla_{\mathbf{r_i}} V(\mathbf{r}) \tag{2.7}$$

where $\mathbf{r}_i$ represents the Cartesian position of every particle i, $\dot{\mathbf{r}}_i$ stands for the time derivative of $\mathbf{r}_i$ and represents the velocity ($\mathbf{v}_i$) of atom i and m_i denotes its mass.

In the classical MD simulations the total exerted force, $\mathbf{F}_i$, on the particle i is given by the interaction potential $V(\mathbf{r})$:

$$\mathbf{F}_i = -\nabla_{\mathbf{r_i}} V(\mathbf{r}) \tag{2.8}$$

Hence, from eq. 2.7 and 2.8 we obtain Newton's equation of motion:

$$\mathbf{F}_i = \dot{\mathbf{p}}_i = m_i \ddot{\mathbf{r}}_i \qquad \Rightarrow \qquad \ddot{\mathbf{r}}_i = \frac{\mathbf{F}_i}{m_i} \qquad\qquad i = 1, 2, ..., N \tag{2.9}$$

where $\ddot{\mathbf{r}}_i$ defines the acceleration of particle i.

To solve these second order differential equations and get the positions and velocities of all the particles of the system we need the initial conditions for $\mathbf{r}_i$ and $\dot{\mathbf{r}}_i$ that are determined in the beginning of the problem.

2.1.3 Numerical solution of equations of motion

In order to solve numerically the equations of motion in every step of the previous algorithm there are some well-known integration methods. A criterion for choosing an integration method is to be relatively accurate, fast and not computationally expensive, which means not to use a large amount of memory space. In addition, it is very important to use an algorithm that respects the energy conservation of the Hamiltonian system and which is time reversible as Newton's equation of motion is. We will mention two numerical integrators: Velocity Verlet and Leapfrog, both variants of general Verlet integrator.

Verlet integrator is a numerical method used to solve Newton's equations of motion. Although, as it is shown below, it is a ″position-only″ scheme and this is why it is not very applicable when velocities or momenta are requested. To generate its formula we determine as $\Delta t > 0$ the time step of the algorithm and we

write Taylor expansion for $\mathbf{r}(t)$ at $(t+\Delta t)$ and $(t-\Delta t)$, where $\mathbf{r}'(t), \mathbf{r}''(t), \mathbf{r}'''(t)$ denote, correspondingly, the first, second and third time derivative:

$$\begin{aligned}\mathbf{r}(t+\Delta t) =& \mathbf{r}(t) + \mathbf{r}'(t)(t+\Delta t - t) + \\ &\frac{\mathbf{r}''(t)(t+\Delta t - t)^2}{2!} + \frac{\mathbf{r}'''(t)(t+\Delta t - t)^3}{3!} + \mathcal{O}(\Delta t^4)\end{aligned} \tag{2.10}$$

$$\begin{aligned}\mathbf{r}(t-\Delta t) =& \mathbf{r}(t) + \mathbf{r}'(t)(t-\Delta t - t) + \\ &\frac{\mathbf{r}''(t)(t-\Delta t - t)^2}{2!} + \frac{\mathbf{r}'''(t)(t-\Delta t - t)^3}{3!} + \mathcal{O}(\Delta t^4)\end{aligned} \tag{2.11}$$

Consequently:

$$\mathbf{r}(t+\Delta t) = \mathbf{r}(t) + \mathbf{v}(t)(\Delta t) + \frac{\mathbf{a}(t)(\Delta t)^2}{2} + \frac{\mathbf{b}(t)(\Delta t)^3}{6} + \mathcal{O}(\Delta t^4) \tag{2.12}$$

$$\mathbf{r}(t-\Delta t) = \mathbf{r}(t) - \mathbf{v}(t)(\Delta t) + \frac{\mathbf{a}(t)(\Delta t)^2}{2} - \frac{\mathbf{b}(t)(\Delta t)^3}{6} + \mathcal{O}(\Delta t^4) \tag{2.13}$$

By the summation of equations 2.12 and 2.13:

$$\mathbf{r}(t+\Delta t) + \mathbf{r}(t-\Delta t) = 2\mathbf{r}(t) + \mathbf{a}(t)(\Delta t)^2 + O(\Delta t^4) \tag{2.14}$$

we get the final scheme of general Verlet integrator:

$$\mathbf{r}(t+\Delta t) = 2\mathbf{r}(t) - \mathbf{r}(t-\Delta t) + \mathbf{a}(t)(\Delta t)^2 + O(\Delta t^4) \tag{2.15}$$

In the above equations and in what follows in the chapter:
$\mathbf{r}(t)$ is the position in time t,
$\mathbf{v}(t)$ the velocity in time t,
$\mathbf{a}(t)$ the acceleration in time t,
$\mathbf{b}(t)$ is a notation for the third derivative of $\mathbf{r}(t)$ with respect to the time and $\mathcal{O}(\Delta t^4)$ is the order of the error of the approximation.

Verlet algorithm does not require the velocity to compute the new position. However, one can derive the velocity from the difference of equations 2.12-2.13:

$$\mathbf{r}(t+\Delta t) - \mathbf{r}(t-\Delta t) = 2\mathbf{v}(t)\Delta t + O(\Delta t^3) \tag{2.16}$$

or:

$$\mathbf{v}(t) = \frac{\mathbf{r}\,(t+\Delta t) - \mathbf{r}\,(t-\Delta t)}{2\Delta t} + O(\Delta t^3) \tag{2.17}$$

Therefore, for calculating the velocity using equation 2.17 we should know the position at next time which means that we cannot calculate both position

and velocity in the same time step. In order to avoid this problem we present two derivatives of the Verlet integrator.

Velocity Verlet integrator is one of the most widespread methods. The advantage over classical Verlet is that this one incorporates velocity in the same time step as position. The formula goes as follows:

$$\mathbf{r}(t+\Delta t) = \mathbf{r}(t) + \mathbf{v}(t)\Delta t + \frac{\mathbf{F}(t)\Delta t^2}{2m} \tag{2.18}$$

$$\mathbf{v}(t+\Delta t) = \mathbf{v}(t) + \frac{\mathbf{F}(t) + \mathbf{F}(t+\Delta t)}{2m}\Delta t \tag{2.19}$$

We have to make clear that instead of acceleration $\mathbf{a}(t)$ we write $\frac{\mathbf{F}}{m}$ just to mention that $\mathbf{a}(t)$ is calculated from the interaction potential using $\mathbf{r}(t)$ and not from $\mathbf{v}(t)$, so $\mathbf{v}(t+\Delta t)$ can be calculated independently without the calculation of $\mathbf{a}(t+\Delta t)$.

Leapfrog integrator, follows the formula:

$$\mathbf{r}(t+\Delta t) = \mathbf{r}(t) + \mathbf{v}(t+\frac{1}{2}\Delta t)\Delta t \tag{2.20}$$

$$\mathbf{v}(t+\frac{1}{2}\Delta t) = \mathbf{v}(t-\frac{1}{2}\Delta t) + \frac{\mathbf{F}(t)\Delta t}{m} \tag{2.21}$$

Note that the initial velocity that we need for the integration in this case is $\mathbf{v}(t-\frac{1}{2}\Delta t)$ instead of $\mathbf{v}(t)$ and firstly the velocity at half a time step is calculated (eq. 2.21). Then, the positions in whole step are calculated (eq. 2.20) with respect to the half-time step velocity. Which means that, corresponding to equation 2.21, the velocity at this step is given by:

$$\mathbf{v}(t+\Delta t) = \mathbf{v}(t) + \frac{\mathbf{F}(t+\frac{1}{2}\Delta t)}{m}\Delta t \tag{2.22}$$

The advantage of this algorithm is that it is less complicated, so it requires less storage than velocity Verlet [23].

2.1.4 Thermostats and Barostats

The previous method addresses the solution of classical equations of motion in the microcanonical statistical ensemble (NVE), where number of simulated atoms (N), volume of the simulated system (V) and total energy of the system(E) are been kept constant. In this case the total energy of the system, in Cartesian coordinates, is been described by its Hamiltonian:

$$H(\dot{\mathbf{r}}, \mathbf{r}) = K(\dot{\mathbf{r}}) + V(\mathbf{r}) \tag{2.23}$$

with $K(\dot{\mathbf{r}})$ standing for the total kinetic energy of the system and $V(\mathbf{r})$ the potential energy.

However, sometimes there is a need to evolve a molecular system under specific conditions of temperature T (isotherm) and/or pressure P (isobaric conditions) [24]. In order to maintain T and P constant we use the appropriate thermostats and barostats, respectively. Below, we present two kinds of thermostats and two types of barostats that are related to the current work.

Nosé-Hoover thermostat

Nosé introduced a new parameter (degree of freedom) s which plays the role of a heat bath aiming to damp out temperature deviations from the desirable level and actually being an additional degree of freedom in the Lagrangian of the system [25]. This new parameter results in one more term in potential energy (noted as V_s) and another one in the total kinetic energy (noted as K_s) giving the following Hamiltonian:

$$H_{Nosé-Hoover}(\dot{\mathbf{r}}, \mathbf{r}) = H(\dot{\mathbf{r}}, \mathbf{r}) + K_s + V_s \tag{2.24}$$

where:

$$K_s = \frac{p_s^2}{2Q} \tag{2.25}$$

for

$$p_s = Q\frac{\dot{s}}{s} \tag{2.26}$$

being the momentum associated with s as well as Q represents the "effective mass" associated with s.
The potential energy with respect to s equals to:

$$V_s = gk_BT\ln s \tag{2.27}$$

with g equals to the total number of degrees of freedom and k_B being the Boltzmann constant.

Berendsen thermostat and barostat

Another way for performing isothermal and/or isobaric MD simulations is to use an extended Lagrangian, by coupling the system into a temperature and/or pressure bath [26]. This is achieved, correspondingly, by the following equations:

$$\frac{dT}{dt} = \frac{1}{\tau_T}(T - T_{ext}) \tag{2.28}$$

$$\frac{dP}{dt} = \frac{1}{\tau_P}(P - P_{ext}) \tag{2.29}$$

where T_{ext} and P_{ext} are the desired temperature and pressure values and τ_T and τ_P are the time constants characterizing the frequency of the system coupling to temperature and pressure baths [24]. The solution of these equations forces velocities and positions to be scaled at every time step by factors x_T and x_P, respectively,with:

$$x_T = \left(1 + \frac{dt}{\tau_T}\left(\frac{T}{T_{ext}} - 1\right)\right)^{\frac{1}{2}} \tag{2.30}$$

$$x_P = 1 - \beta_T \frac{dt}{\tau_P}\left(P - P_{ext}\right) \tag{2.31}$$

Velocity-rescaling thermostat is a Berendsen thermostat with the following, additional, stochastic term that ensures a correct kinetic energy by modifying it according to :

$$dK = (K_0 - K)\frac{dt}{\tau_T} + 2\sqrt{\frac{KK_0}{g}}\frac{dW}{\sqrt{\tau_T}} \tag{2.32}$$

where K is the kinetic energy, g the number of degrees of freedom and dW a Wiener (stochastic) process [27].

Parrinello-Rahman barostat is a pressure coupling method similar to the Nosé-Hoover temperature coupling giving the statistically correct NPT ensemble, using a "pressure bath" [27]. This barostat represents the equation of motion of the matrix $\mathbf{b}$ of the simulation's area vectors:

$$\frac{d^2\mathbf{b}}{dt^2} = V\mathbf{W}^{-1}\mathbf{b}'^{-1}(\mathbf{P} - \mathbf{P}_{ref}) \tag{2.33}$$

where V is the volume of the box, $\mathbf{W}$ is a matrix parameter that determines the strength of the coupling and the matrices $\mathbf{P}$ and $\mathbf{P}_{ref}$ are, respectively, the current and the reference pressure [14].

2.1.5 Langevin Dynamics

By adding a friction and a noise term (random force) in Newton's equation of motion we get the stochastic differential equation:

$$m_i\ddot{\mathbf{r}}_i = \mathbf{F}_i - \zeta\dot{\mathbf{r}}_i + \mathbf{f}_i(t) \tag{2.34}$$

called Langevin equation.
In this equation ζ is the friction coefficient and $\mathbf{f}_i(t)$ is the random force of the media, appearing to be uncorrelated at different times, satisfying the fluctuation-dissipation theorem:

$$\langle f_{i\alpha}(t), f_{i\beta}(t')\rangle = 2k_BT\zeta\delta_{ij}\delta_{\alpha\beta}\delta(t - t') \tag{2.35}$$

where:

$$\delta_{ij} = \begin{cases} 1, & i = j \\ 0, & i \neq j \end{cases} \tag{2.36}$$

and α, β denote Cartesian components [28].

2.2 Molecular Model - Force Field

The equation (2.8) describing the total force acting on a particle i can be expressed as:

$$\mathbf{F}_i = -\nabla_{\mathbf{r_i}} V(\mathbf{r}) \tag{2.37}$$

The total potential $V(\mathbf{r})$ is subdivided in potentials depending on bonded ($V_{\text{bonded}}(\mathbf{r})$) and non-bonded ($V_{\text{non-bonded}}(\mathbf{r})$) interactions:

$$V(\mathbf{r}) = V_{\text{bonded}}(\mathbf{r}) + V_{\text{non-bonded}}(\mathbf{r}) \tag{2.38}$$

assuming that $\mathbf{r} = (\mathbf{r}_1, \mathbf{r}_2, ..., \mathbf{r}_N)$ is the vector of the positions of all the N particles (atoms) in our molecular system.

2.2.1 Bonded interactions

Bonded interactions in a molecular model are defined depending on the number of the atoms that participate in the bond. There are covalent bonds connecting two atoms, angle-bending including three atoms and dihedral angles, where four atoms are included.

In addition, there are two types of dihedral angles. The improper one keeps specific groups in a predefined plane. More specifically, it is a harmonic potential applied to the angle between the two planes consisting the dihedral and keeps these two planes locked. The one without this property is called proper. Therefore, the total potential corresponding to the bonded interaction is calculated as:

$$V_{\text{bonded}}(\mathbf{r}) = V_{\text{bonds}}(\mathbf{r}) + V_{\text{angles}}(\mathbf{r}) + V_{\text{pr.dihedrals}}(\mathbf{r}) + V_{\text{im.dihedrals}}(\mathbf{r}) \tag{2.39}$$

In the following we will discuss the particular functional forms for each component of the potential used in this work.

1. V_{bonds} is a harmonic potential that represents the stretching of a covalent bond of two atoms i an j, as it is shown in Fig. 2.2(a), given by the equation:

$$V_{\text{bonds}}(r_{ij}) = \frac{1}{2} k_{ij} (r_{ij} - r_{ij}^0)^2 \tag{2.40}$$

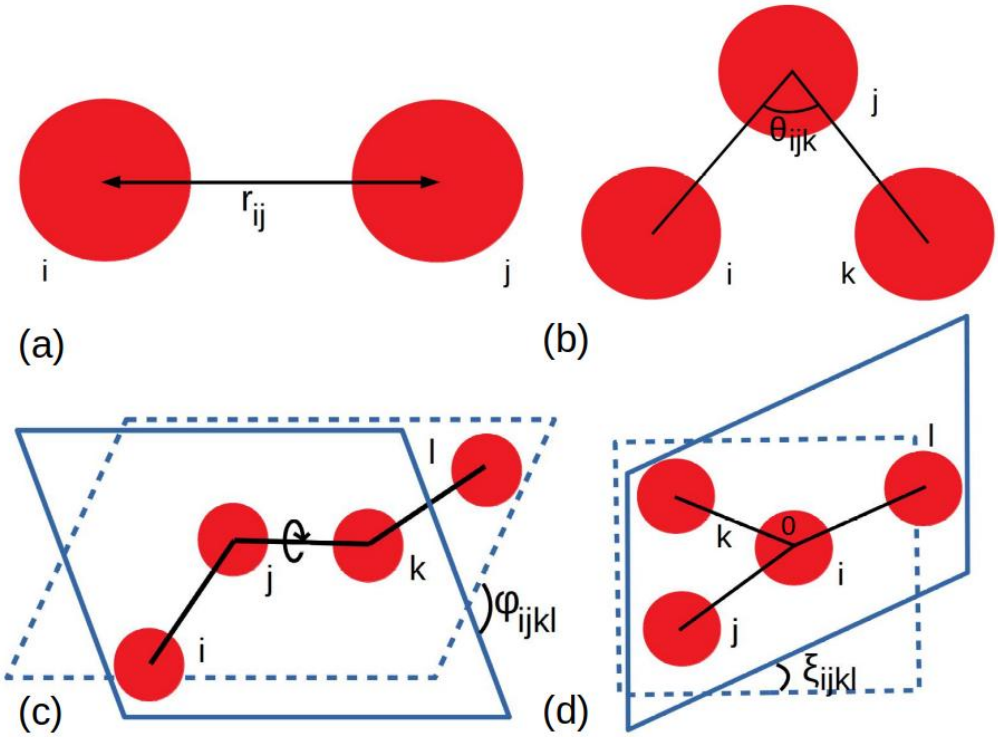

Figure 2.2: (a) Bond between atoms i and j, (b) Angle between atoms i,j,k, (c) Proper dihedral angle between i, j, k, l where the solid line defines the plane going through i, j, k and the dotted line the one through j, k, l (d) Improper dihedral angle between i, j, k, l where the solid line defines the plane going through j, k, l and the dotted line the one through i, j, k.

with $r_{ij} = |\mathbf{r}_i - \mathbf{r}_j| = |\mathbf{r}_{ij}|$ representing the current length of the bond, where $\mathbf{r}_i$ and $\mathbf{r}_j$ are the positions of i and j atom correspondingly.
r_{ij}^0 corresponds to the equilibrium bond length and k_{ij} is the force constant.
The total bond potential of the system is:

$$V_{\text{bonds}} = \sum_{\#\text{ of bonds}} V_{\text{bonds}}(r_{ij}) \tag{2.41}$$

2. V_{angles} represents the overall angle-bending potential and equals to

$$V_{\text{angles}} = \sum_{\#\text{ of angles}} V_{\text{angles}}(\theta_{ijk}) \tag{2.42}$$

where:

$$V_{\text{angles}}(\theta_{ijk}) = \frac{1}{2} k_\theta (\theta_{ijk} - \theta_{ijk}^0)^2 \tag{2.43}$$

is the harmonic potential of angle-bending vibration between the three atoms i,j,k forming the θ_{ijk} angle as it is shown in Fig.2.2(b). θ^0_{ijk} is the corresponding equilibrium angle and k_θ is the angle bending force constant. θ is connected to vectors between atoms through the relation:

$$\cos\theta_{ijk} = \frac{\mathbf{r}_{ij} \cdot \mathbf{r}_{jk}}{r_{ij} r_{jk}} \tag{2.44}$$

3. $\underline{V_{\text{pr.dihedrals}}}$ defines the total potential of the proper dihedrals and it equals to:

$$\sum_{\#\text{ of pr.dihedrals}} V_{\text{pr.dihedral}}(\phi_{ijkl}) \tag{2.45}$$

For the calculation of the dihedral potential between i,j,k,l atoms we use two types of equations, depending on the type of the particular atoms:

- The periodic form:

$$V_{\text{pr.dihedral}}(\phi_{ijkl}) = k_\phi(1 + \cos\left(n\phi_{ijkl} - \phi^0_{ijkl}\right) \tag{2.46}$$

where ϕ_{ijkl} is the angle between the planes ijk and jkl (see Fig. 2.2.(c)) which satisfies:

$$\cos\phi = -\frac{(\mathbf{r_{ij}} \times \mathbf{r_{jk}}) \cdot (\mathbf{r_{jk}} \times \mathbf{r_{kl}})}{|\mathbf{r_{ij}} \times \mathbf{r_{jk}}||\mathbf{r_{jk}} \times \mathbf{r_{kl}}|} \tag{2.47}$$

ϕ^0_{ijkl} is the corresponding equilibrium angle and k_ϕ the proper dihedral constant.

- The cosine series form (Ryckaert-Bellemans) according to which :

$$V_{\text{pr.dihedrals}}(\phi_{ijkl}) = \sum_{n=0}^{5} C_n \left(\cos\left(\phi_{ijkl} - \pi\right)\right)^n \tag{2.48}$$

with C_n for $n = 1, 2, 3, 4, 5$ being a prefactor in $kJmol^{-1}$ units.

4. $\underline{V_{\text{im.dihedrals}}}$ defines the harmonic potential of the improper dihedrals of the system (see Fig. 2.2(d)), given by:

$$V_{\text{im.dihedrals}} = \sum_{\#\text{ of im.dihedrals}} \frac{1}{2} k_\xi (\xi_{ijkl} - \xi^0_{ijkl})^2 \tag{2.49}$$

with ξ_{ijkl} representing the angle between the planes ijk and jkl, ξ^0_{ijkl} is the corresponding equilibrium angle and k_ξ the improper dihedral constant.

2.2.2 Non-bonded interactions

The non-bonded potentials are responsible for the intermolecular interactions that do not include any kind of covalent bonds, like Van der Waals and electrostatics.

Van der Waals is distance-dependent, attractive at long distance and repulsive at short distance, interaction between pairs of atoms. To describe this kind of interaction we use the Lennard-Jones potential (V_{LJ}). Correspondingly, electrostatic interactions between charged atoms are described by the Coulomb potential (V_{C}).

The total potential energy due to the non-bonded interactions is separated into these two terms:

$$V_{\mathrm{non-bonded}} = V_{\mathrm{LJ}} + V_{\mathrm{C}}. \tag{2.50}$$

Lennard-Jones interactions

LJ potential describes the pair interactions with respect to the distance r_{ij} between the pairs by the equation:

$$V_{\mathrm{LJ}}(r_{ij}) = 4\epsilon_{ij}\left(\left(\frac{\sigma_{ij}}{r_{ij}}\right)^{12} - \left(\frac{\sigma_{ij}}{r_{ij}}\right)^{6}\right). \tag{2.51}$$

The parameters σ_{ij} and ϵ_{ij} can be derived from the parameters characteristic for each atom i and j by using the combination rule:

$$\sigma_{ij} = \frac{1}{2}\left(\sigma_i + \sigma_j\right), \epsilon_{ij} = \sqrt{\epsilon_i \epsilon_j} \tag{2.52}$$

The parameters σ_i , ϵ_i for every particle i are known from experimental data, or quantum mechanics calculations. Note that σ_i represents the atomic diameter of the atom i.

In eq. 2.51 the attractive, Van der Waals, interactions are presenting by the term: $-\left(\frac{\sigma_{ij}}{r_{ij}}\right)^6$. The repulsion term $\left(\frac{\sigma_{ij}}{r_{ij}}\right)^{12}$ has been added in the potential because of the fact that two atoms i, j cannot penetrate each other when they come at a distance smaller than the one of the sum of their atomic radii ($\frac{\sigma_i}{2} + \frac{\sigma_j}{2} = \sigma_{ij}$).

Hence, for $r_{ij} > \sigma_{ij}$ the force between i and j atoms is attractive, however, for $r_{ij} >> \sigma_{ij}$ the two atoms are too far to interact which means that LJ potential energy is close to zero (see Fig. 2.3). On the other hand, for $r_{ij} < \sigma_{ij}$ this force becomes repulsive and as r_{ij} gets closer to zero the LJ potential energy goes to infinity because of the overlap of the atoms. In the exact point where $r_{ij} = \sigma_{ij}$ the potential energy is zero. There is also a point where $r_{ij} = 2^{\frac{1}{6}}\sigma_{ij}$ where LJ potential reaches its minimum value, called depth of LJ well: $-\epsilon_{ij}$.

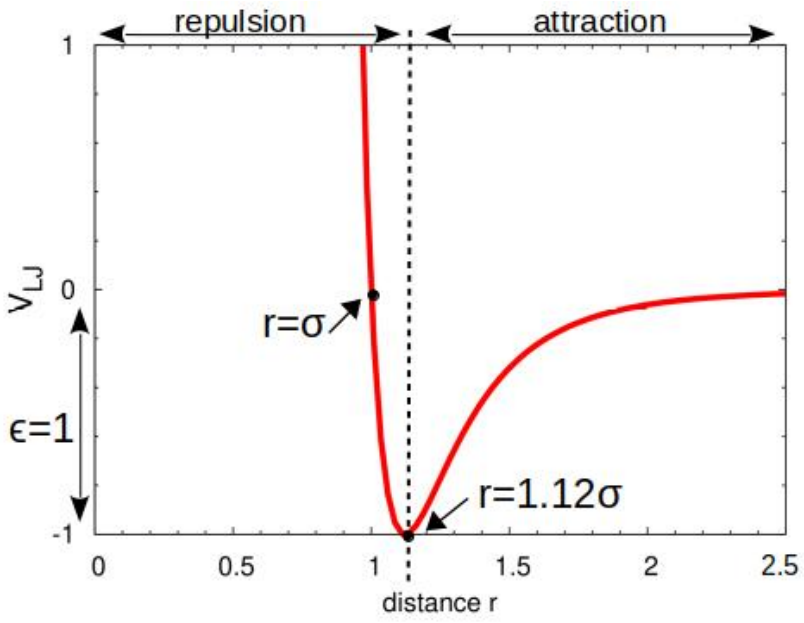

Figure 2.3: Lennard-Jones potential for chosen $\sigma = \epsilon = 1$.

Coulomb interactions

For two particles (atoms) i and j with distance r_{ij} between them and corresponding charges Q_i and Q_j, their electrostatic Coulomb interaction is calculated by:

$$V_{\mathrm{C}}(r_{\mathrm{ij}}) = \frac{Q_i Q_j}{4\pi\epsilon_0\epsilon_r r_{\mathrm{ij}}} \tag{2.53}$$

where ϵ_0 is the vacuum electric permittivity and ϵ_r the dimensionless relative permittivity of the media.

However, for each atom in our simulated systems $Q_i = 0$, thus, there are no Coulomb interactions.

2.3 Periodic Boundary Conditions (PBC)

A real life's system consists of a huge number of atoms of the order of the Avogadro number ($\mathrm{N_{Av}} = 6.023 \times 10^{23}$). In order to work in smaller system and mimic the behavior of a macroscopic system, we need to approximate this large system by a smaller one. This is achieved by applying periodic boundary conditions. Namely, we separate the whole space in smaller cells and study just

one of them, the so called ″simulation box″ in which the number of particles is fixed at N. All the other cells around the specific cell are just the exact copies of the simulation box, as it is shown in Fig. 2.4.

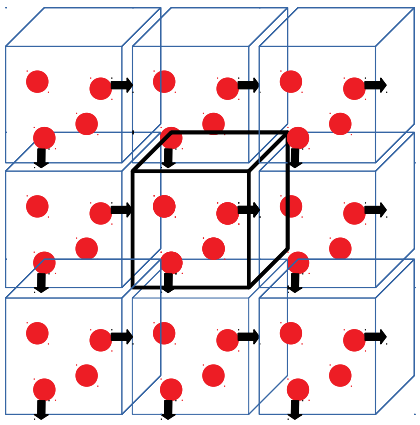

Figure 2.4: Schematic representation of the periodic boundary conditions. The simulation box is painted with thick lines, the boxes surrounding the simulation box are its copies.

For a better understanding, we explain it on an example. Periodic boundary conditions define positions of each moving particle in a way that no particle is ″allowed to leave the box″. When one particle goes out of the box's limit, the condition puts an image of it back in the box at a corresponding periodic position, or, in other words, its periodic image enters the box.

The problem here is that when we study the interactions of an atom in our box with all the other atoms around it, it is possible that the interactions with an atom j and at the same time with its periodic image are taken into account. To avoid the above problem, we apply the minimum image convention (see Chap. 2.5) and truncate the short-range interactions as it is discussed in the cut-off sections below.

2.4 Cut-off and tail corrections

As molecular dynamics is a computational method, there is a need to use techniques that reduce the computational cost while at the same time do not affect the accuracy. The most expensive calculations, in our problem, are force

calculations. In order to decrease this computational cost we define a cut-off distance (radius) r_{cut} and in the calculations of the pair potential (eq. 2.51) only the interactions between atoms whose mutual distance is smaller than r_{cut} are taken into account. By applying this method we compute a smaller amount of non-bonded interactions resulting in the significant reduction of the cost. We can now reformulate eq. 2.51 to the following:

$$V_{\text{LJ}}(r_{ij}) = \begin{cases} 4\epsilon_{ij}\left(\left(\frac{\sigma_{ij}}{r_{ij}}\right)^{12} - \left(\frac{\sigma_{ij}}{r_{ij}}\right)^{6}\right), & r_{ij} \leq r_{\text{cut}} \\ 0 \qquad\qquad\qquad\qquad\quad , & r_{ij} > r_{\text{cut}} \end{cases} \tag{2.54}$$

However, in order to minimize the error that would be produced by taking into account only short-range interactions, we have to choose a sufficiently large value for r_{cut}, but also smaller than $\frac{L}{2}$. The contribution of the particles with $r_{ij} > r_{\text{cut}}$ for a potential $V(r)$ is estimated with the so-called tail corrections [14]:

$$V_{\text{tail}} = 2\pi\rho \int_{r_{\text{cut}}}^{\infty} V(r) r^2 dr \tag{2.55}$$

and for the special case of homogeneous system of atoms interacting via a Lennard-Jones potential it is given from [14]:

$$V_{\text{LJ}_{\text{tail}}} = \frac{8}{3}\pi\rho\left[\frac{1}{3}\left(\frac{1}{r_{\text{cut}}}\right)^{9} - \left(\frac{1}{r_{\text{cut}}}\right)^{3}\right] \tag{2.56}$$

where ρ corresponds to the average number density.

According to this, eq. 2.54 is been reformed again to:

$$V_{\text{LJ}}(r_{ij}) = \begin{cases} 4\epsilon_{ij}\left(\left(\frac{\sigma_{ij}}{r_{ij}}\right)^{12} - \left(\frac{\sigma_{ij}}{r_{ij}}\right)^{6}\right), & r_{ij} \leq r_{\text{cut}} \\ \frac{8}{3}\pi\rho\left[\frac{1}{3}\left(\frac{1}{r_{\text{cut}}}\right)^{9} - \left(\frac{1}{r_{\text{cut}}}\right)^{3}\right], & r_{ij} > r_{\text{cut}} \end{cases} \tag{2.57}$$

From eq. 2.55 it is obvious that the only case for the V_{tail} to be finite is if $V(r)$ function decays more rapidly than r^{-3} (in three dimensions). This condition is satisfied if the long-range interaction between molecules is dominated by dispersion forces [14]. This is the reason why cut-off distance, tail correction and minimum image convention (see below) can be applied to Lennard-Jones potential. On the other hand, all three of them are inapplicable to Coulomb interactions where the tail correction diverges and the interactions between all periodic images should be taken into account.

2.5 Minimum Image Convention

Because of the huge number of atoms in the system and their infinite periodic images, for all the interactions between the reference atom i and an atom j we choose the closest image of j to i. Therefore, in every direction of the three dimentional space, we find an image of j in the periodic boxes which fulfills:

$$x_{ij} < \frac{L}{2}, \quad y_{ij} < \frac{L}{2}, \quad z_{ij} < \frac{L}{2}$$

where x_{ij}, y_{ij}, z_{ij} correspond to the distances between two atoms i and j in directions x, y, z of the space, respectively. L stands for the length of the simulation box.

Consequently, as the distance between two atoms i and j is defined as $r_{ij} = \sqrt{x_{ij}^2 + y_{ij}^2 + z_{ij}^2}$, r_{ij} cannot be larger than $\sqrt{3}\frac{L}{2}$.

3. Generation and equilibration of model systems

In the current work we are interested in studying and predicting structure-properties relations of symmetric, star-shaped, polystyrene (PS) polymers. Star-shaped polymers are, in other words, linear chains attached to a common branch point. In our work the ″branch point″ is not represented by a single atom, but by a dendritic structure consisted of various atoms which, from now on, we call kernel. Every star is characterized by the number of arms named functionality f and the arm length. In our study we perform atomistic MD simulations for a variety of functionalities, in two different types of systems. The exact characteristics of the systems as well as the whole simulation process are introduced in this chapter.

3.1 Description of the systems

We simulate polystyrene (PS) star-shaped polymers which consist of a dendritic structure (kernel) and a specific number of polystyrene arms attached to it. More specifically, the kernel structure is composed of carbon units connected in a way it is illustrated in Fig. 3.1. In both sketches every enumerated ball represents a chemical carbon unit as follows: number 1 is the central carbon C unit and next generations are CH units except from the last one which represent the CH_2 units. The f arms are then joined to the last generation, i.e., to the CH_2 units. The number of atoms in each dendritic structure depends on the functionality and is summarized in Tab. 3.1. In terms of the arms, each one of them can be thought as a linear PS chain of 40 monomeric units attached to the kernel and terminated with the CH_3 group. It means, that every arm has the same length, we only vary the number of arms (f). Accordingly, the notation $(PS)_f$ will be used from now on in order to specify each star with respect to functionality f.

The two types of systems under investigation are: (a) melts composed of 15 $(PS)_f$ stars of the same functionality f and (b) blends composed of one $(PS)_f$

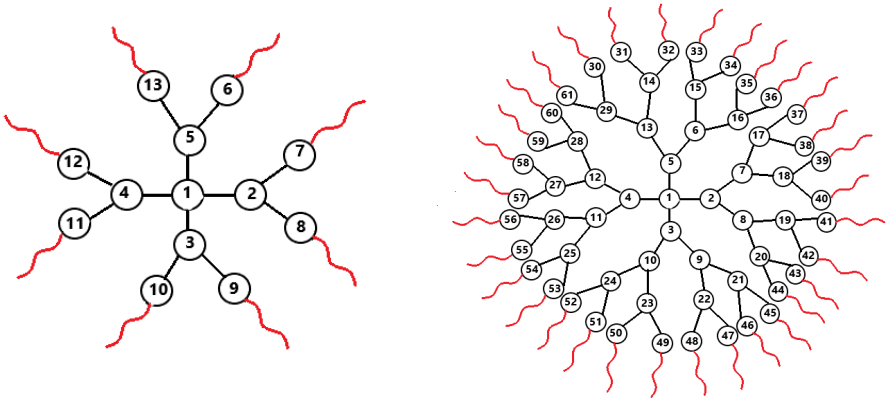

Figure 3.1: Sketch of the dendritic kernel of (a) $(PS)_8$ and (b) $(PS)_{32}$ with the corresponding numbering of atoms. The red tails represent the attached arms.

star and a specific number of PS linear chains with the same length as the star's arms, i.e., 40 monomeric units. The number of the linear chains is chosen in such way that all the blend systems have the same weight fraction (wt%): 0.097.

For the comparison we also simulate one reference system of only linear chains in melt and two more melts with stars of functionality 8 and 16, respectively, with the kernel from the star of functionality 32 labeled as $(PS)_{f/61}$. At the dendritic structure of Fig.3.1(b), for $(PS)_{8/61}$ we attached an arm to every fourth carbon unit of the last generation, e.g., 31, 35, 39 etc. Similarly, every second carbon unit in $(PS)_{16/61}$ has an arm connected to it, e.g., 31, 33, 35 etc.

The interactions between all the atoms are defined through the atomistic force field. We use the united-atom model of TRAPPE force field [29]. The united-atom model means that the hydrogens are not simulated explicitly but are included together with the carbon in one unit, for example CH unit of PS ring (for the structure of PS unit see Chapter 1 Fig. 1.1). The advantage of this approach is that it reduces the number of atoms which we need to simulate, thus the total number of interactions that need to be calculated. Namely, in our model, every monomer is composed of 8 united atoms (from now on we refer to them as atoms), so every arm contains 40×8 atoms plus 1 terminal carbon

CHARACTERISTICS OF SIMULATED SYSTEMS					
SYSTEM	**f**	**number of atoms in the kernel**	**number of stars**	**number of linear chains**	**number of atoms in the system**
linear	0	0	0	250	80250
blend $(PS)_8$	8	13	1	75	26656
blend $(PS)_{16}$	16	29	1	105	38870
blend $(PS)_{32}$	32	61	1	298	105991
melt $(PS)_4$	4	5	15	0	19335
melt $(PS)_8$	8	13	15	0	38715
melt $(PS)_{16}$	16	29	15	0	77475
melt $(PS)_{32}$	32	61	15	0	154995
melt $(PS)_{8/61}$	8	61	15	0	39435
melt $(PS)_{16/61}$	16	61	15	0	77955

Table 3.1: Characteristics of systems under investigation.

unit corresponding to the CH_3 group, in total 320+1=321 atoms. Each linear chain has the same number of atoms. The number of atoms in the simulation box for all the systems is listed in Tab. 3.1.

The specific constants for bonded and non-bonded interactions (see Sec. 2.2 and equations 2.40, 2.43, 2.46, 2.48, 2.49, 2.51, 2.53 for the functional forms of the potentials used in this work) for TRAPPE force field can be found in the literature and are reported in the Appendix: Tab. 6.1 and Tab. 6.2 [29].

3.2 System preparation and equilibration

In order to study the structural properties of the systems first we need to reach a state where the configuration will be independent from the initial one. This state is the equilibrium state and the process to reach it is called equilibration. In Fig. 3.2 we present the scheme with all the steps which we followed during the equilibration procedure. For all our simulations we use the GROMACS [27] simulation package. Also, all the simulation runs were performed by parallel programming on the Fujitsu workstation in our group, with 12 nodes. Up to 4 nodes have been used, each containing 24 Intel(R) Xeon(R) processors.

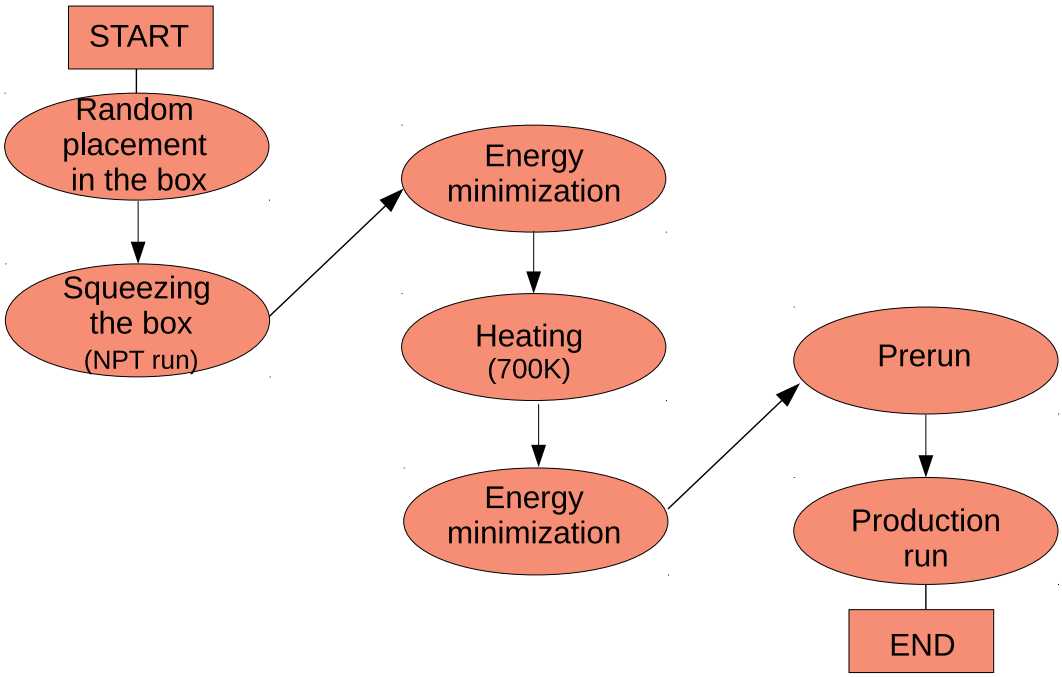

Figure 3.2: Scheme of the used simulation processes for the proper equilibration of the model star systems.

The procedure follows the steps below:

Step 1:
We start from an initial configuration. For the purpose of avoiding the overlaps of atoms, in this configuration, the arms are fully stretched when attaching to the kernel. In Fig. 3.3 we show the snapshots of the initial configurations of two selected stars. These snapshots have been taken after attaching the arms and performing energy minimization procedure that is explained below.

Step 2:
The prepared stars are randomly placed in a box which size was bigger than the one related on the final melt conditions. More specifically, the box was big enough to avoid overlaps between molecules.

Step 3:
We run a NPT simulation which squeezes the box till the system reaches the referred density. It means, that we applied Berendsen barostat, which keeps

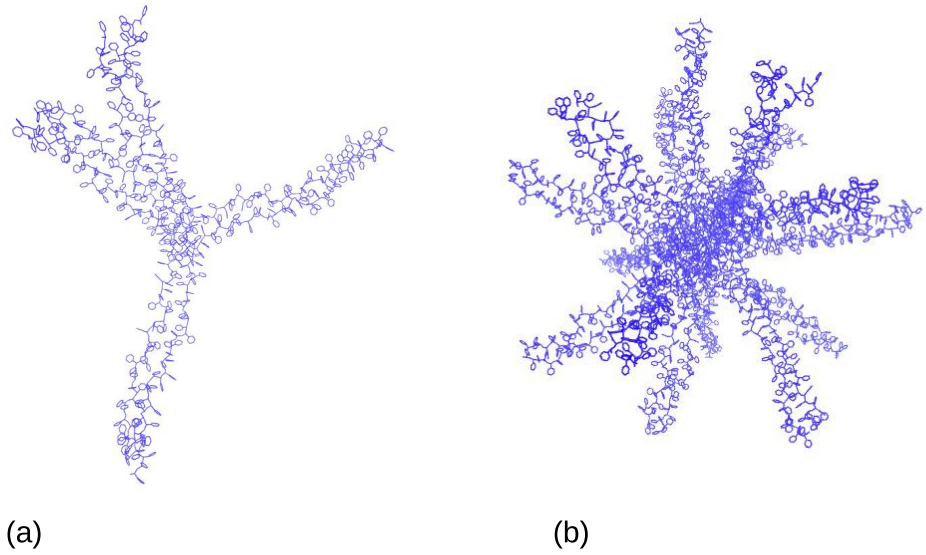

Figure 3.3: Snapshot of the initial configuration of (a) $(PS)_8$ and (b) $(PS)_{32}$ star.

the pressure constant at 1.0 atm, and the v-rescale thermostat to maintain the temperature at 600K.

Step 4:
We apply energy minimization in between the simulation runs in order to correct some possible configurations with stretched bonds, that can be present due to a very close packing of the atoms close to the dendritic structure. Through this process we get a configuration that corresponds to the minimum possible energy.

Step 5:
To speed up the relaxation of the material we applied a heating procedure using again Barendsen barostat and set the temperature to 700K. In this run, Langevin dynamics are used.

Step 6: We apply, again, energy minimization process in order to correct any possible stretches of the bonds.

Step 7:

After the heating, we run a pre-production run. The settings used in this run are the same as those for the production run, i.e., the same barostat and thermostat (see in the next section). However, the data from this run are not included in the examined trajectory, as the system needs some time to adjust to the given temperature, which is lower that the one in the previous step of the equilibration (i.e., heating). The length of the pre-production run was approximately 50 ns.

Step 8:
After this whole procedure our systems are fully equilibrated and we can export all the information we need in order to examine their behavior through the quantities of our interest.

Step 9:
The number of steps of the whole production run equals to 10^8 with time step 0.001 ps which means that the run lasts 10^5 ps or, equivalently, 100 ns. The temperature during the production run for our systems is 600K. Therefore, we apply Nosé-Hoover thermostat to keep the temperature around this value and Parrinello-Rahman barostat for a constant pressure of 1 atm. In order to make sure that our systems are well-equilibrated we check the stability of the thermodynamical properties such as temperature, energy, density etc. The results from the study of internal distances (see Chap. 4.1.1) is another evidence of a well-equilibrated system.

4. Results

The main goal of every MD simulation is to collect information about the evolution in time under specific conditions of the system under study. To quantify the behavior of system components we use a set of quantities which help us to describe the properties of the system. In this section we present some of them and we also discuss their comparison to the theoretically predicted behavior. In this work we study only static properties, which means that they are independent of time. In other words, our results do not depend on the choice of the time window in which they were measured during the production run. In a system in equilibrium the static properties fluctuate around their average values during the whole simulation run. The mean values of all quantities presented in this section were obtained by averaging over all stored configurations of the systems, i.e., we used every frame of the exported trajectory to calculate the average properties.

4.1 Structural properties

4.1.1 Internal Distances

We start with the examination of the possible internal deformation of the molecules in our systems. This deformation can be a consequence of a bad packing of monomers during the equilibration procedure. In order to do that we calculate internal distances along the arms in the stars or along the linear chain. The quantity measures the mean-square end-to-end extension $\langle R^2 \rangle(n)$ of a chain segment including n bonds:

$$\langle R_n^2 \rangle = \langle ||\mathbf{r}_{i+n} - \mathbf{r}_i||^2 \rangle \tag{4.1}$$

where $\langle \cdot \rangle$ represent the statistical average over all possible pairs of atoms along the arm/chain separated by n bonds. The statistics is improved by averaging over all arms or chains in the system. This quantity has been used to check the internal deformations in the melts of linear entangled chains [30]. The entangled chains consist of many monomeric units (more than 10 times longer than

those in our work) and their equilibration is very time consuming. Auhl *et al.* presented a method to speed up the equilibration process and they showed that any possible internal deformation of the chains during the process is reflected in the plot of $\langle R_n^2 \rangle / n$. The same quantity was reported in simulations of entangled stars using a bead spring model [31].

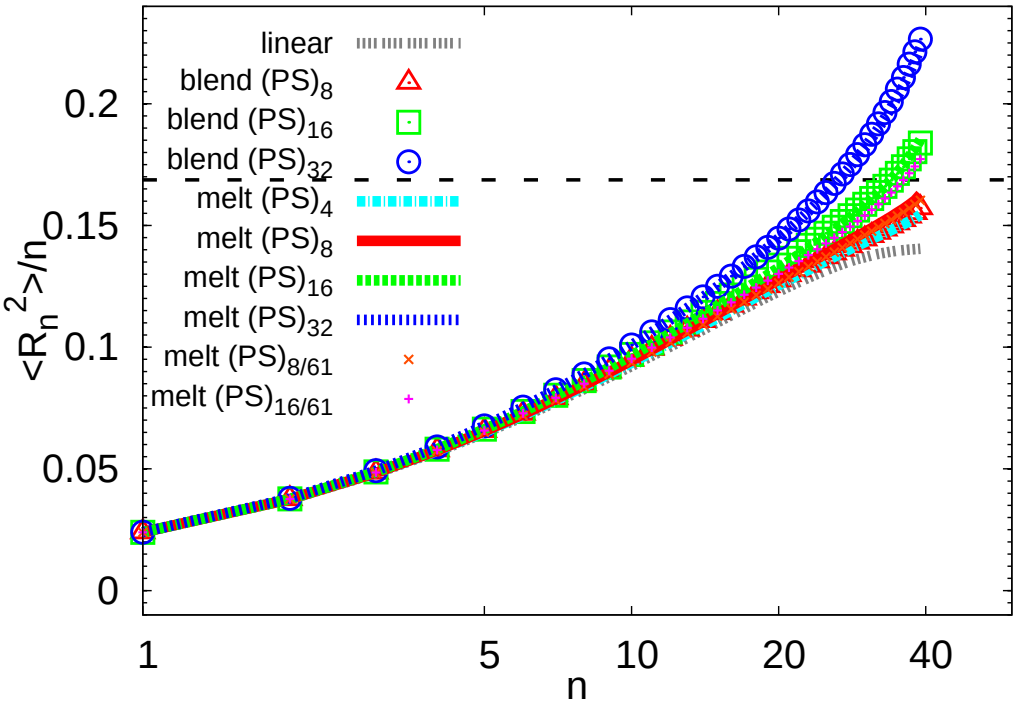

Figure 4.1: Internal distances $\langle R_n^2 \rangle / n$ of all systems.

In Fig. 4.1 we present $\langle R_n^2 \rangle$ divided by the number of bonds n for all studied systems. There is no indication of the deformation at short distances ($n < 20$) which would be manifested by a peak in this area. First comparing the blends (triangles, squares, and circles) with melts (lines of the corresponding colors), we observe that the data in Fig. 4.1 for these two types of systems overlap. The data for the linear chains are systematically under the curves for the star arms, i.e., the arms of stars are stretched in comparison to linear chains. By comparing the stars of different functionality, it is obvious that with increasing the functionality of the star the stretching of the arms at long distances ($n > 20$) is much more pronounced.

In the ideal case of a long Gaussian chain of a length N_{chain}, the eq. 4.1 is related to the stiffness of the chain through the following equation [32]:

$$\langle R^2 \rangle = C_\infty N_{\text{chain}} b^2 \tag{4.2}$$

where b is an average bond length and C_∞ is a characteristic ratio. The Gaussian chain represents a model of an ″ideal″ flexible chain with the uncorrelated motion of bond vectors. In reality this motion is not uncorrelated and the chain behaves as Gaussian at length scales much bigger than the bond length. The characteristic ratio, C_∞, is a quantity that measures the stiffness [2] and its values for common polymers can be found in literature [33]. Only for the cases of very long chain lengths (arms) C_∞ could be obtained from an asymptotic plateau of the $\langle R_n^2 \rangle / n$ plot. In Fig. 4.1 the dashed line represents the estimation of the value of C_∞ for polystyrene at 600K [33], which corresponds to the temperature in our simulation. It is apparent from Fig. 4.1 that there is no plateau observed for our systems.

4.1.2 Radius of Gyration

Radius of gyration, R_g, is a structural measure about the compactness of the molecule and gives us the opportunity to provide estimation of the molecular size. R_g is defined by the formula:

$$R_g = \sqrt{R_g^2} \tag{4.3}$$

where:

$$R_g^2 = \frac{\sum\limits_i ||\mathbf{r}_i - \mathbf{r}_{cm}||^2 m_i}{\sum\limits_i m_i}, \tag{4.4}$$

m_i is the mass of particle i, $\mathbf{r}_i$ is its position, $\mathbf{r}_{cm}$ is the position of the center of mass of the measured object (here a star polymer molecule).
For the purpose of our study we calculate two types of this quantity: (a) $R_{g_{mol}}$ and (b) $R_{g_{arm}}$. The first one represents the radius of gyration of the whole molecule. $R_{g_{arm}}$ corresponds to the radius of gyration of a single arm of the star (i.e., $i = 1, 2, ..., 321$) and, in this case, $\mathbf{r}_{cm}$ represents the center of mass of one arm. In Fig. 4.2 we show a schematic representation of the measurement of (a) $R_{g_{mol}}$ and (b) $R_{g_{arm}}$ quantities on a snapshot of a randomly selected star.

It has been proposed [34] that for chains obeying Gaussian statistics (ideal chains), the radius of gyration of the molecule is related to the radius of gyration of a single arm through Zimm-Stockmayer equation [32]:

$$\frac{\langle R_{g_{mol}}^2 \rangle}{\langle R_{g_{arm}}^2 \rangle} = \frac{3f - 2}{f}. \tag{4.5}$$

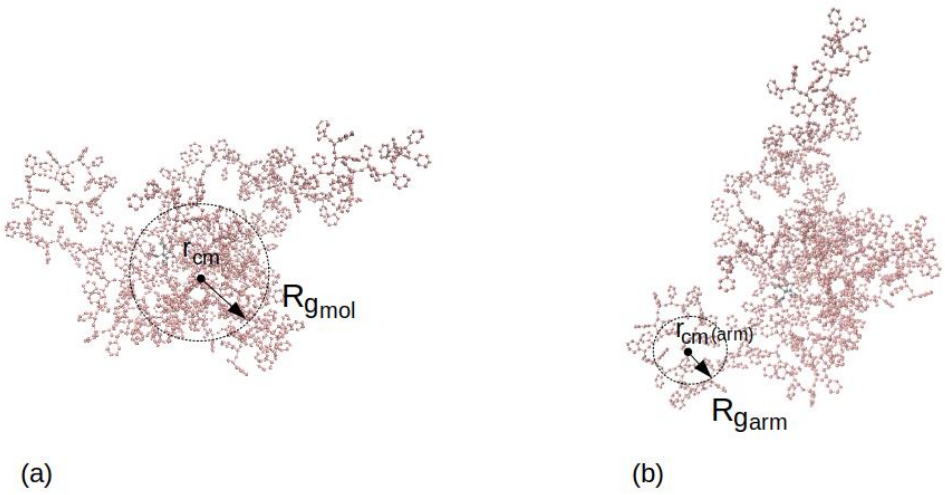

Figure 4.2: Schematic representation of the measurement of (a) $R_{g_{mol}}$ and (b) $R_{g_{arm}}$ quantities on a snapshot of a randomly selected star of functionality $f = 8$.

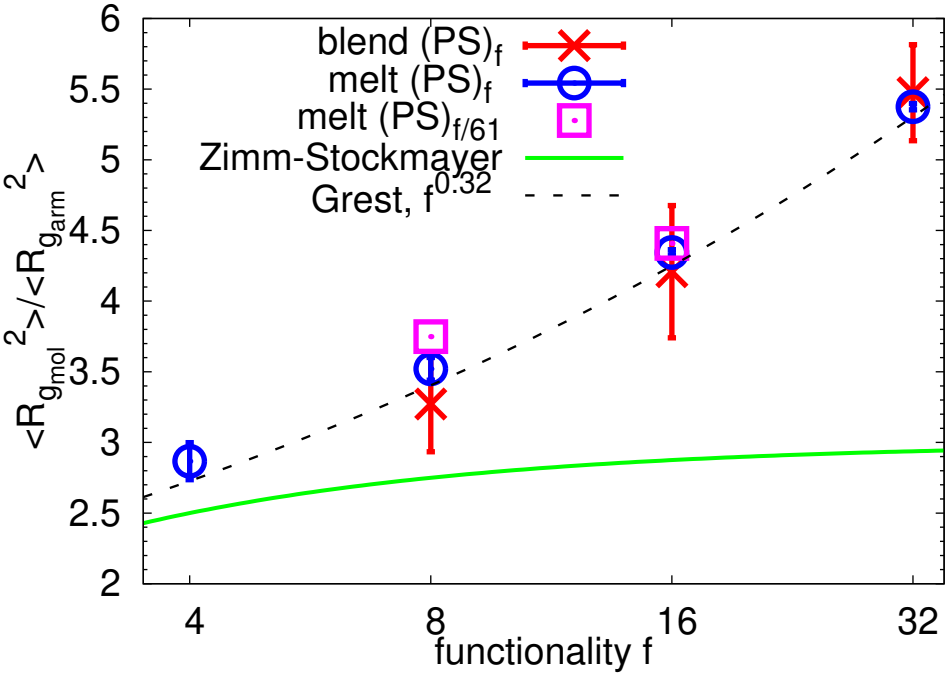

Figure 4.3: Comparison of our data with Zimm-Stockmayer prediction.

For coarse-grained models and experimental results for stars in θ conditions

a power low relation has been found [35]:

$$\frac{\langle R^2_{g_{mol}} \rangle}{\langle R^2_{g_{arm}} \rangle} \sim f^{\alpha}. \tag{4.6}$$

For stars in θ conditions the exponent $\alpha = 0.32$ [35].

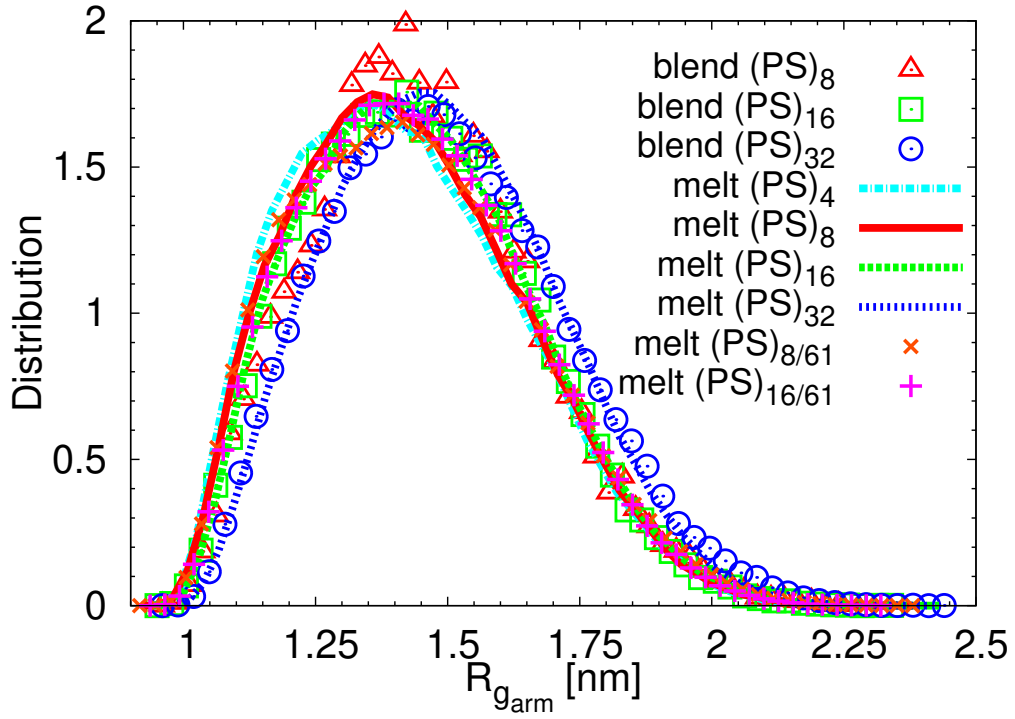

Figure 4.4: Distributions of the radius of gyration of the arms ($R_{g_{arm}}$) of all systems.

In Tab. 4.1 we present the averages of $\sqrt{\langle R^2_{g_{mol}} \rangle}$ and $\sqrt{\langle R^2_{g_{arm}} \rangle}$ for each one of our systems under investigation with the corresponding error. For simplicity we define: $R_{g_{mol}} = \sqrt{\langle R^2_{g_{mol}} \rangle}$.

The error bars have been estimated as follows: first we used the block method, i.e., we divided the trajectory into 4 blocks (time windows), we calculated the property for each block (R^2_g) and obtained the error bar as a standard deviation between the mean value from the whole trajectory ($\langle R^2_g \rangle$) and the values obtained from the blocks. The number of the blocks (4) has been chosen empirically.

According to propagation of errors of precision analysis [36], the error ΔZ of a quantity $Z = X^k$ with known error ΔX of the quantity X is calculated by

Average values of $R_{g_{mol}}$ and $R_{g_{arm}}$		
SYSTEM	$R_{g_{mol}}$ [nm]	$R_{g_{arm}}$ [nm]
blend $(PS)_8$	2.63 ± 0.07	1.45 ± 0.037
blend $(PS)_{16}$	2.97 ± 0.088	1.45 ± 0.021
blend $(PS)_{32}$	3.51 ± 0.047	1.50 ± 0.026
melt $(PS)_4$	2.40 ± 0.03	1.43 ± 0.154
melt $(PS)_8$	2.68 ± 0.015	1.49 ± 0.008
melt $(PS)_{16}$	3.01 ± 0.002	1.52 ± 0.002
melt $(PS)_{32}$	3.45 ± 0.004	1.55 ± 0.001
melt $(PS)_{8/61}$	2.78 ± 0.18	1.43 ± 0.23
melt $(PS)_{16/61}$	3.02 ± 0.1	1.44 ± 0.17

Table 4.1: Average values of $R_{g_{mol}}$ and $R_{g_{arm}}$ with the corresponding error (standard deviation).

the formula:

$$\Delta Z = kX^{k-1}\Delta X \tag{4.7}$$

The corresponding formula for the calculation of the error $\bar{R}_g$ (standard deviation) of $\sqrt{\langle R^2_{g_{mol}}\rangle}$ and $\sqrt{\langle R^2_{g_{arm}}\rangle}$, reported in Tab. 4.1, for $k = \frac{1}{2}$, is given by:

$$\bar{R}_g = \frac{1}{2}\langle R^2_g\rangle^{-0.5}\bar{R}^2_g \tag{4.8}$$

where $\bar{R}^2_g$ is the standard deviation obtained from the block method.

In Fig. 4.3 we plot the ratio $\langle R^2_{g_{mol}}\rangle/\langle R^2_{g_{arm}}\rangle$ and compare our data to the above-mentioned predictions. The relation proposed by bead spring simulations [35], $\langle R^2_{g_{mol}}\rangle/\langle R^2_{g_{arm}}\rangle \sim f^{0.32}$, is plotted as a guide to the eye only and does not correspond to the fit of the data. We observe that all three types of systems do not agree with Zimm-Stockmayer prediction, however, they seem to follow a power law. This power law seems to be very close to the one predicted by Grest *et al.* [35] (see the dashed line in Fig.4.3).

In Fig. 4.4 we plot the distributions of instantaneous values of $R_{g_{arm}}$ for all the systems. The differences between different types of systems (i.e., melts, blends and with modified kernel) and systems with different functionalities are

barely noticeable. The distributions are fairly Gaussian with small deviations at small values of $R_{g_{arm}}$.

4.1.3 Asphericity and prolateness

In order to get information about the shape of the PS stars in each system we introduce two shape parameters: asphericity (a) and prolateness (p). We obtain these parameters from radius of gyration tensor (S), whose elements are defined as follows:

$$S_{\alpha\beta} = \frac{1}{N_{\text{star}}^2} \sum_{i=1}^{N_{\text{star}}} (r_\alpha^i - r_\alpha^{cm})(r_\beta^i - r_\beta^{cm}) \tag{4.9}$$

where N_{star} is the number of the atoms of one molecule (star) and α and β are Cartesian coordinates of the tensor S in three dimensions, i.e., α, β=x,y,z. Correspondingly, r_α^i and r_β^i represent the components of the vector $\mathbf{r}_i$. Let us define the eigenvalues of the tensor in a way $\lambda_1 < \lambda_2 < \lambda_3$. Then, asphericity a and prolateness p parameters are calculated by the formula:

$$a = \frac{(\lambda_2 - \lambda_1)^2 + (\lambda_3 - \lambda_1)^2 + (\lambda_3 - \lambda_2)^2}{2(\lambda_1 + \lambda_2 + \lambda_3)^2} \tag{4.10}$$

and

$$p = \frac{(2\lambda_1 - \lambda_2 - \lambda_3)(2\lambda_2 - \lambda_1 - \lambda_3)(2\lambda_3 - \lambda_1 - \lambda_2)}{2(\lambda_1^2 + \lambda_2^2 + \lambda_3^2 - \lambda_1\lambda_2 - \lambda_1\lambda_3 - \lambda_2\lambda_3)^{\frac{3}{2}}} \tag{4.11}$$

correspondingly.

The values of asphericity range between 0 and 1. For totally spherical shape ($\lambda_1 = \lambda_2 = \lambda_3$) asphericity equals to 0 and the more the shape deviates from a sphere the closer a gets to 1. Prolateness, that fluctuates between -1 and 1, shows how oblate or prolate an object is. Value $p = -1$ implies a perfectly oblate shape where $\lambda_1 < \lambda_2 = \lambda_3$ while for prolate shapes ($\lambda_1 = \lambda_2 < \lambda_3$) the value is $p = 1$. In Fig. 4.5 we present (a) oblate, (b) spherical and (c) prolate shapes for the corresponding values of prolateness p and asphericity a.

Fig. 4.6 and 4.7 show the distributions of asphericity and prolateness of the stars in each one of our systems, respectively.

Between the two types of systems (blends vs. melts) the differences are almost negligible, however, stars in blends appear to be systematically more spherical (Fig. 4.6(a)). In case of $(\text{PS})_{f/61}$ stars we do not notice any differences between the corresponding $(\text{PS})_f$ in melts (Fig. 4.6(b)).

Both of the shape parameters are affected by the functionality f of the stars. The higher the functionality the more the shape of the star approximates a sphere. If we focus our attention on $(\text{PS})_4$ star it is obvious that it is the only

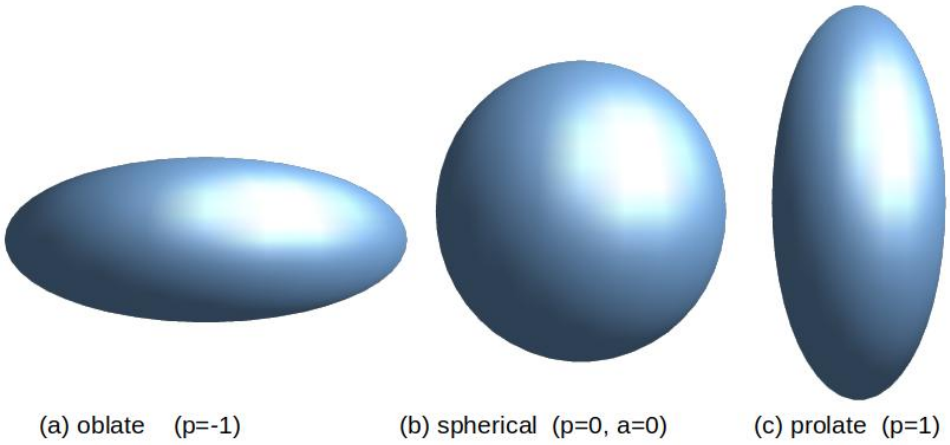

Figure 4.5: Schematic representation of (a) oblate shape for value of prolateness $p = -1$, (b) spherical shape for $p = 0$ and value of asphericity $a = 0$ and (c) prolate shape for $p = 1$.

one with such a wide a distribution (Fig. 4.6(b)) and in terms of prolateness parameter (Fig. 4.7(b)) the only one with the maximum of the distribution at $p = 1$ which reveals the prolate shape of this star and not a spherical one. As the functionality increases ($f \geq 8$) the stars begin to be more spherical. It means that the maximum of the a distribution gets closer to zero till $f = 32$, where the stars look like spheres (Fig. 4.6(b)). For these functionalities, p distributions (Fig. 4.7(b)) do not exhibit any particular maximum (just slightly higher values in the range of $0.5-1$ for $f = 8$), i.e., neither oblate nor prolate shape is present, which is also an indication about the almost-spherical shape for higher f. The more spherical shape of stars with higher functionality is obvious also from Fig. 4.8, where we present snapshots of randomly selected configurations of stars in melts.

4.1.4 Density profile

Another important structural property that we investigate is density profile. Density profile gives us the information about how the atoms of the star distribute to defined radial layers around the central carbon C of the star dendritic kernel, i.e., it calculates the density within one molecule with respect to the distance d from the center of the star. Fig. 4.9 shows a schematic division of the space around the star into spherical layers.

For our study we divide the space around each star into 100 radial layers of the same width up to a distance of $\frac{\sqrt{3}L}{2}$, where L is the simulation box length. In Fig. 4.10 we present the data. The density is plotted with respect

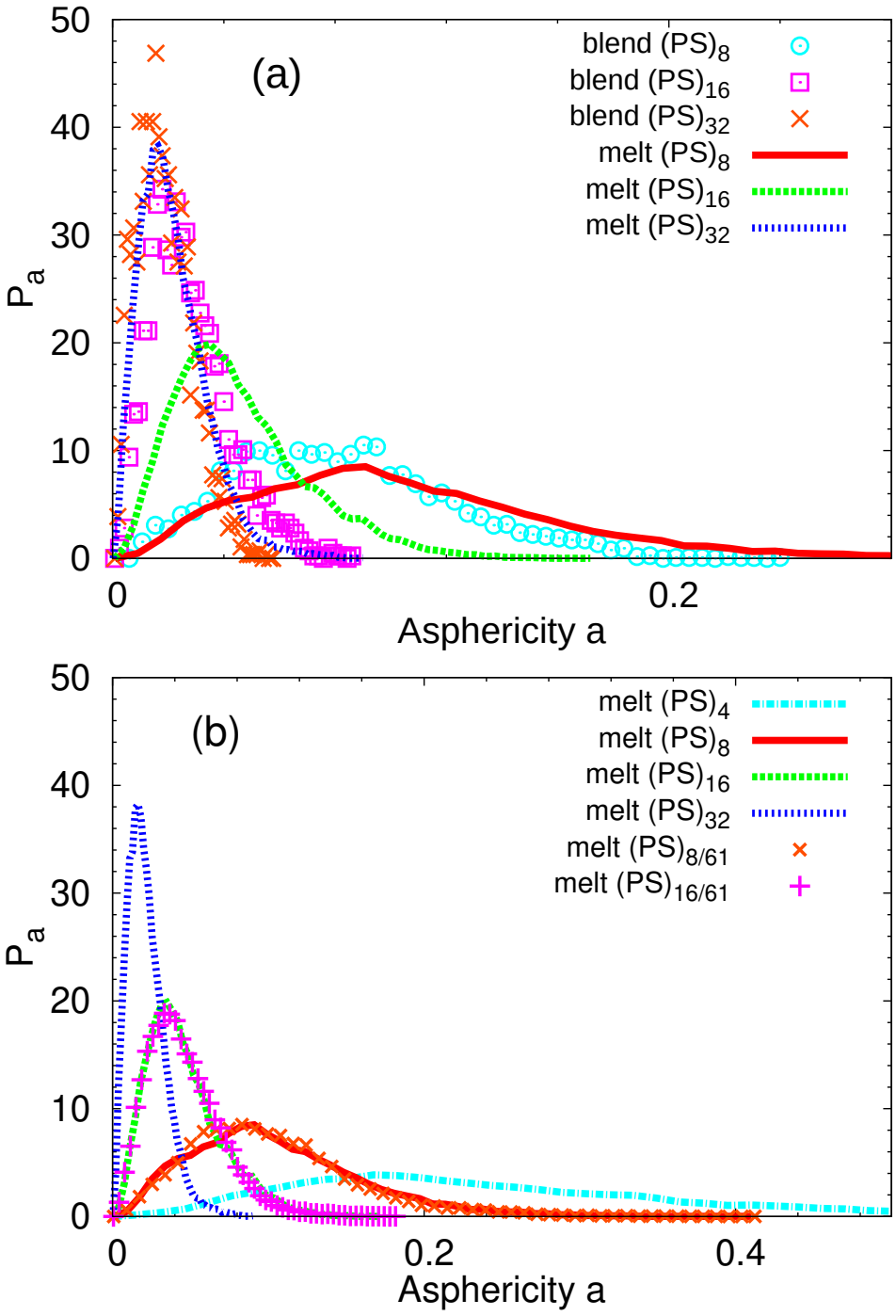

Figure 4.6: Probability distribution of asphericity of (a) blend vs. melt systems and (b) melt systems with different f and kernel.

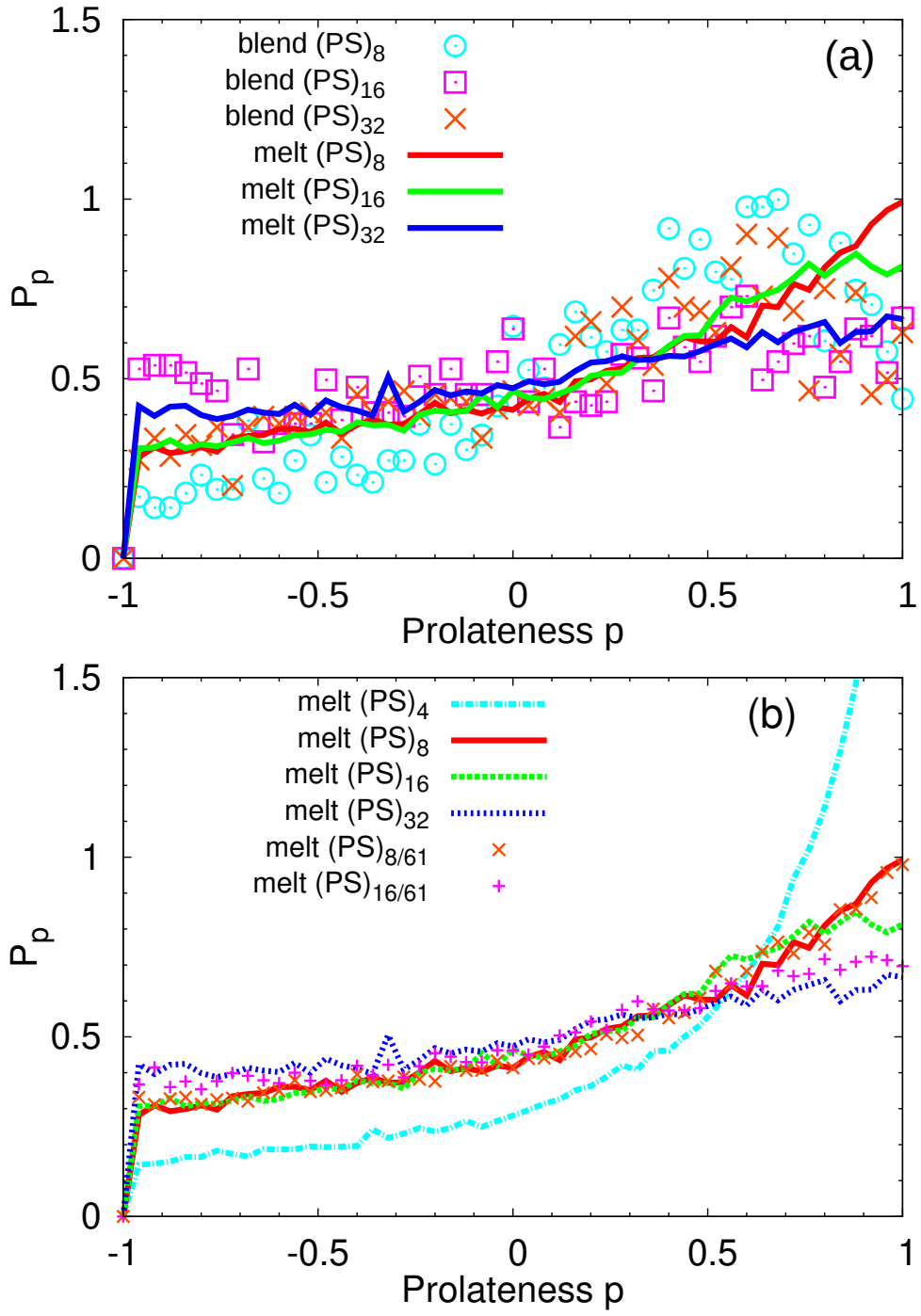

Figure 4.7: Probability distributions of prolateness of (a) blend vs. melt systems and (b) melt systems with different f and kernel.

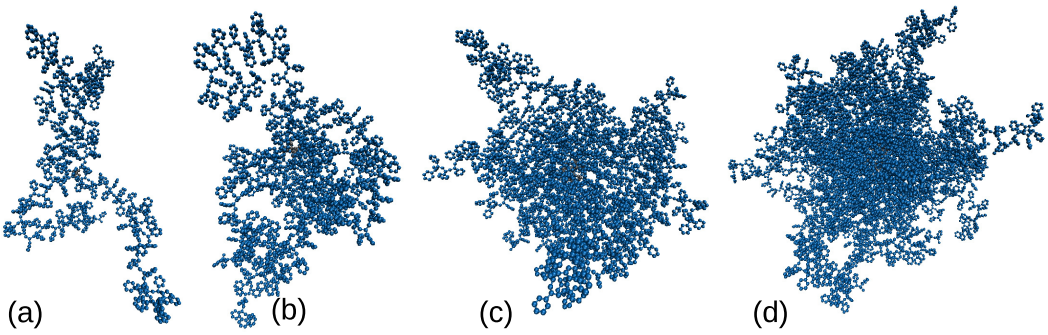

Figure 4.8: Snapshots of a randomly selected configuration of (a) $(PS)_4$, (b $(PS)_8$, (c) $(PS)_{16}$, (d) $(PS)_{32}$. The central dendritic structure is painted gray and PS atoms blue.

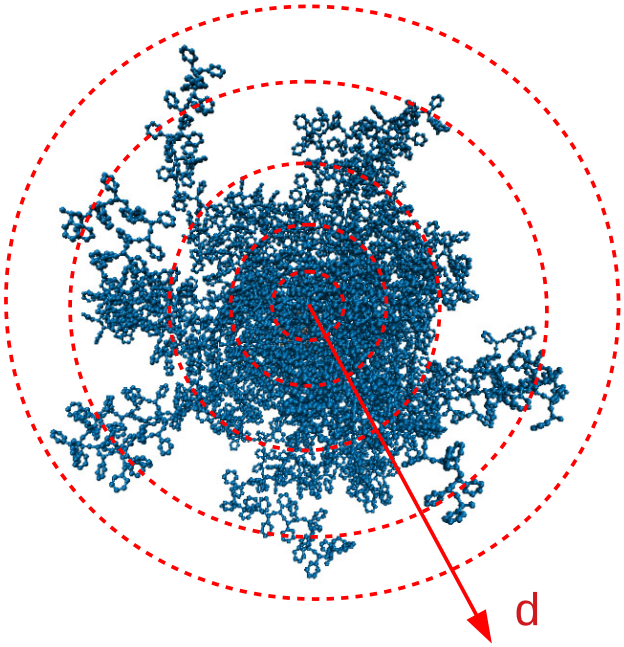

Figure 4.9: Sketch of defined, radial layers around the central atom of the star's kernel in order to calculate the density distribution in each one of them.

to $d/R_{g_{mol}}$ for a better comparison. Moreover, in the graph we only present the data corresponding to the arms, i.e. the atoms of the dendritic structure are not included in the profile. In other words, in this representation the first radial layer $d = 0$ has been shifted to the surface of the dendritic kernel, i.e.,

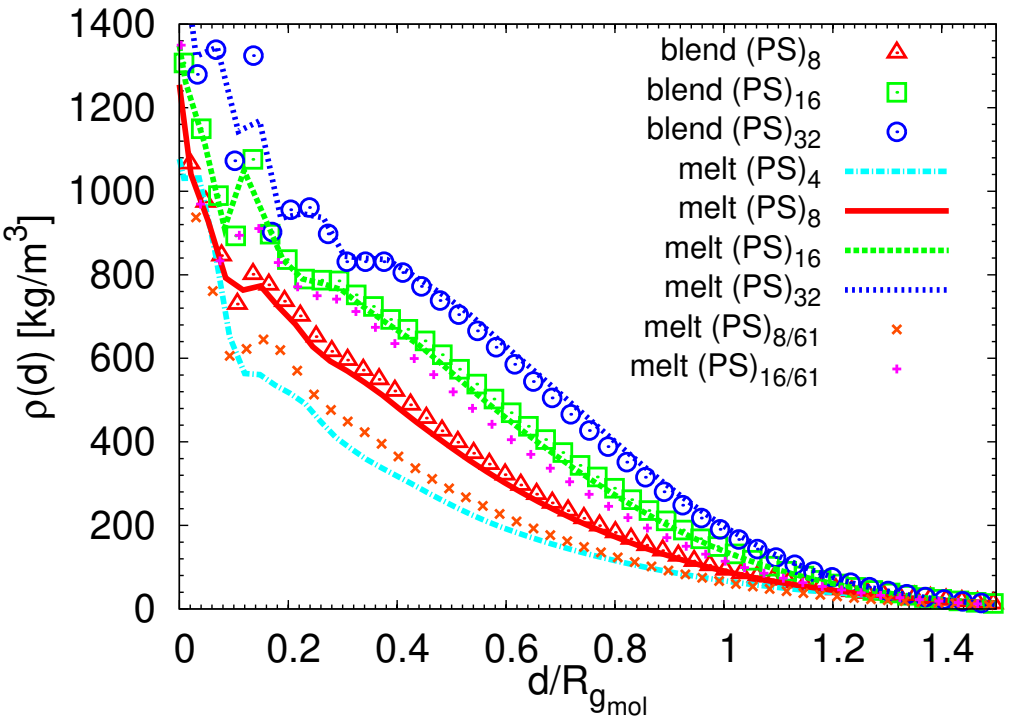

Figure 4.10: Density profiles of all systems.

SYSTEM	**Average density (kg/cm^3)**
blend $(PS)_8$	0.91386 ± 0.000023
blend $(PS)_{16}$	0.914399 ± 0.000014
blend $(PS)_{32}$	0.915386 ± 0.000013
melt $(PS)_4$	0.91886 ± 0.000033
melt $(PS)_8$	0.921437 ± 0.000029
melt $(PS)_{16}$	0.926656 ± 0.00002
melt $(PS)_{32}$	0.936125 ± 0.000017
melt $(PS)_{8/61}$	0.921884 ± 0.00005
melt $(PS)_{16/61}$	0.924738 ± 0.000023
linear	0.913206 ± 0.000014

Table 4.2: Table of average densities of every system.

to the distance $d_k + \sigma/2$, where d_k is the distance of CH_2 atom of the last generation from the central C in the dendritic kernel (see Fig. 3.1) and σ is its LJ diameter. The density profiles in Fig. 4.10 are decaying functions of the

distance d. The density at short distances is higher than the corresponding average densities of the systems (see Tab. 4.2). The values of $d/R_{g_{mol}}$ defining the region of the higher density depend on the functionality, i.e., the higher the f the more extensive is the region of the higher density.

Between blends of star and linear chains and melts we do not observe any significant differences. The density profile of $(PS)_{8/61}$ star attains lower values than the one of $(PS)_8$. However, the data of $(PS)_{16/61}$ almost overlap with those of $(PS)_{16}$.

4.1.5 Center-of-mass pair distribution function

The pair probability distribution function of star centers-of-mass (cm), $g_{cm}(d)$, is proportional to the probability of finding the center-of-mass of a molecule at a distance d from the center-of-mass of a given molecule. It is a quantity that characterizes the mutual positions of the stars in a melt and their penetrability. By penetrability we mean the ability of two stars to come to a close contact. To calculate this quantity we use the equation below:

$$g_{cm}(d) = \frac{M_{\mathrm{cm}}[d, d+\Delta d]}{\Delta V[d, d+\Delta d]} \tag{4.12}$$

where $M_{\mathrm{cm}}[d, d+\Delta d]$ is the number of the centers-of-mass of the stars of the system (except from the given one) in a specific radial layer of width Δd, $\Delta V[d, d+\Delta d]$ is the volume of the radial layer. Then, in order to normalize this quantity in a way that the area under the curve (integral) equals to 1, we divide it by $\int_0^{\frac{L}{2}} g_{cm}(d)\ \mathrm{d}d$.
Hence, we set:

$$g_{cm}(d) \rightarrow \frac{g_{cm}(d)}{\int_0^{\frac{L}{2}} g_{cm}(d)\ \mathrm{d}d} \tag{4.13}$$

and in Fig. 4.11 (a) we plot the $g_{cm}(d)$ distributions of melt systems. As in blends there is only one star per system, there are not data from those systems. In this graph we observe that for low functionalities ($f = 4, 8$) the probability of finding cm-cm distances smaller than the corresponding $R_{g_{mol}}$ is non-zero (see Tab.4.1 for the values of $R_{g_{mol}}$). This means that the centers of mass of these stars can approach very close to each other, which can be interpreted as meaning that $(PS)_4$ and $(PS)_8$ are easily penetrable. For higher functionalities no such phenomenon is present. There are no distances between centers of mass smaller than $R_{g_{mol}}$, so the stars with ($f > 8$) can not be easily penetrable. For a better understanding of the $g_{cm}(d)$ with respect to $R_{g_{mol}}$, in Fig. 4.12, we present the data with the distances d divided by $R_{g_{mol}}$. As $d = R_{g_{mol}}$ corresponds to the point 1 on the x-axis, the above observation becomes more obvious.

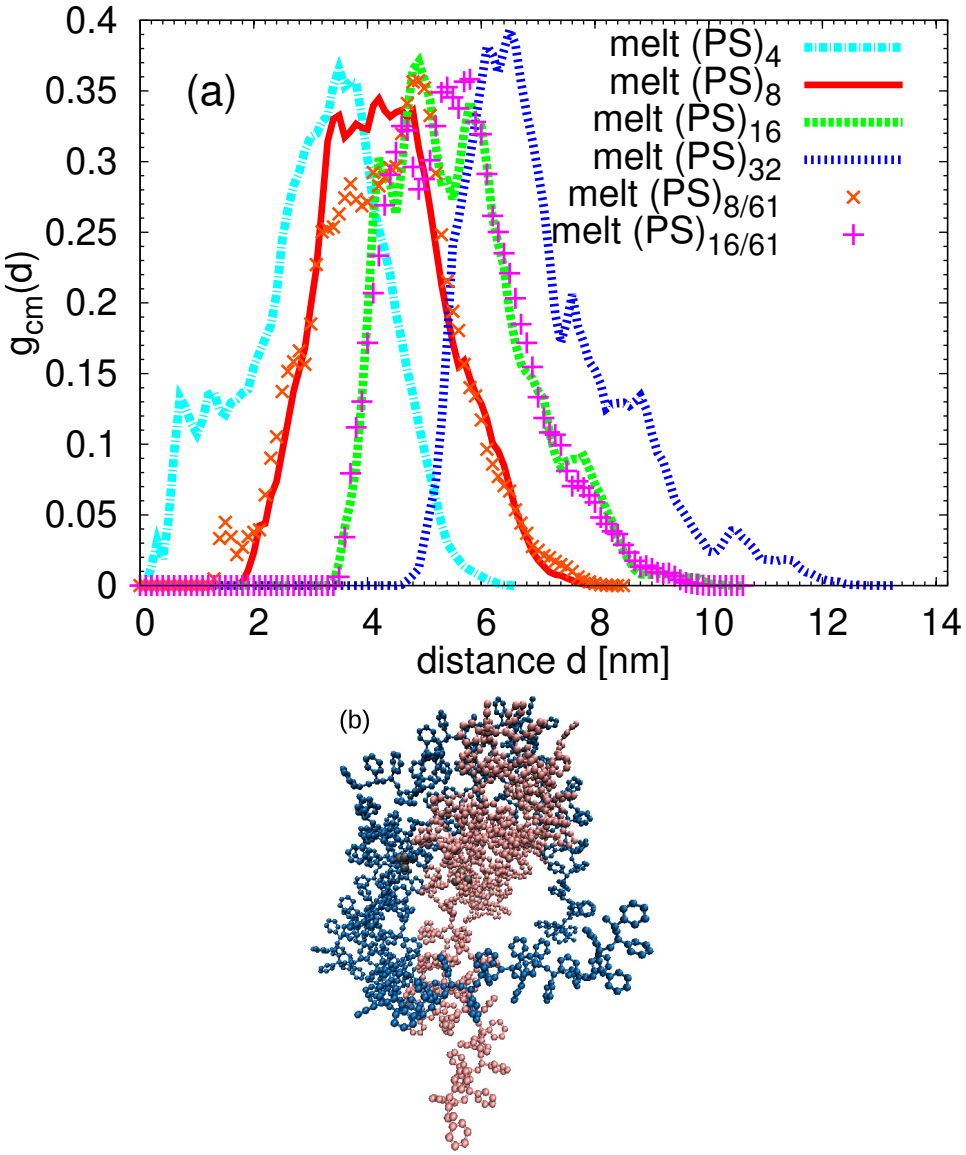

Figure 4.11: (a) Radial distribution of the distances of centers-of-mass of stars in the melts. (b) Example of an alignment of two stars in $(PS)_4$ melt.

In Fig. 4.11(b) we present a representative snapshot of two $(PS)_4$ stars being in a close contact. Due to their prolate shape they can align like two ellipsoids.

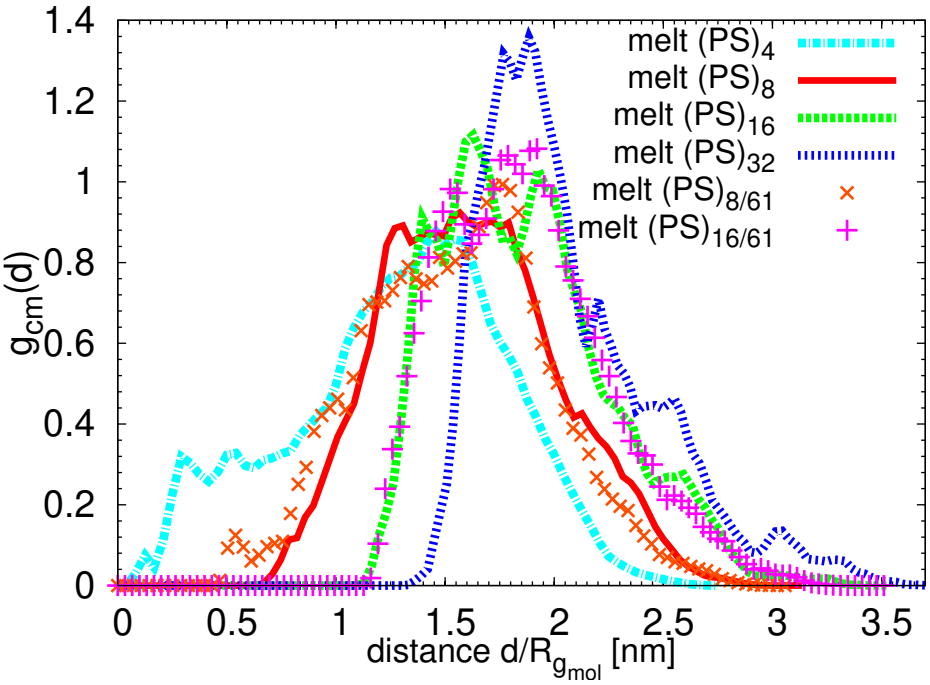

Figure 4.12: Radial distribution of the distances of centers-of-mass of stars in the melts as a function of $\frac{d}{R_{g_{mol}}}$.

4.2 Estimation of the core region

One of the main goals of this study is to identify the functionality of star-shaped polymers, above which they start behaving like soft colloid particles. Concerning the theoretical description of the star-polymer properties, Daoud and Cotton, in 1981, predicted their properties using scaling theory [10]. They proposed a model, the so-called blob model, giving the conformation of a star-shaped polymer by taking into account the radial variation of the monomer concentration. Defining d the distance from the center of the star, according to this model, the inner structure of the star is regarded as a succession of concentric shells of blobs, each blob in the shell having size $\xi(d)$ like it is shown in Fig. 4.13 [32]. Within each blob every chain behaves as there are no effects of the neighboring chains. By purely geometrical arguments, it follows that the size of the blob scales as $\xi(d) \sim df^{-1/2}$ and in relation to d the star is separated into three regions: (a) the core ($d < d_c$), (b) the unswollen region ($d_c < d < d'$) in the middle and (c) the swollen one in the end of the star ($d > d'$). Apart from other factors such as monomer length, the values of d_c and d' depend on the environment (media) around the star (good/bad solvent, melt etc.). In melts, that are systems with high density and no solvent, only the unswollen region

and the core are observable.

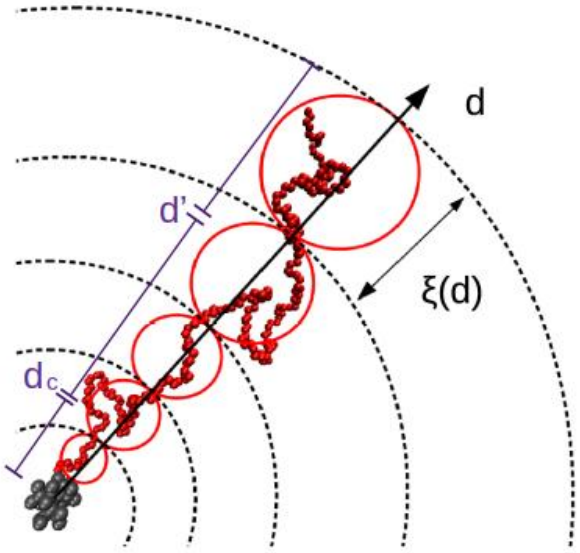

Figure 4.13: Schematic representation of Daoud and Cotton blob model. Each blob in the shell has size $\xi(d)$ where d is the distance from the center of the star, d_c defines the core region ($d < d_c$), d' defines the swollen region ($d > d'$) and the middle (unswollen) region corresponds to $d_c < d < d'$.

The core is defined to be the region around the center of the star that cannot be penetrated from atoms of different molecule [10]. In this region, the blob size equals to the monomer size and the corresponding parts of the arms are fully stretched. The scaling argument indicates that the radius of the core region scales as

$$d_c \sim f^{1/2} l \tag{4.14}$$

where l stands for the persistence length of the polymer. The persistence length is related to the stiffness of the chain and the characteristic ratio (See eq. 4.2).

In an experimental work [11], eq. 4.14 is used for the estimation of the radius of the core region of $(PS)_f$ for l=0.73 nm. It is also shown that the transition to colloidal behavior is due to the increasing core fraction:

$$\frac{d_c}{R_{g_{mol}}} \tag{4.15}$$

where $\langle R^2_{g_{mol}} \rangle \sim \frac{3f-2}{f^2} \langle R^2_{g_{lin}} \rangle$ and $R_{g_{lin}}$ represents the radius of gyration of linear polystyrene taken from literature (note the difference from eq. 4.5 where instead

of $R_{g_{lin}}$ C.Likos suggested $R_{g_{arm}}$ [32]). Increasing the core fraction means that for high f the core region occupies larger volume fraction of the star. Specifically, the value of functionality that the star-shaped polymers begin to behave like colloids seems to be $f > 8$ for the experimental systems presented in ref. [11].

Another core estimation for a general model of star-shaped polymers came from a simulation work using the density profile of the system. Pakula [12] *et al.* used a lattice model for multiarm star-shaped polymers in melts and showed that the density profile can be approximated by a Gaussian distribution with its center at the center of mass of the star. Then, the radius of the core d_c was defined as the separation of the maximum of the Gaussian from the center of mass of the star.

Having these studies in mind, in this chapter, we calculate some relevant quantities in order to achieve the estimation of the impenetrable core region of the star with respect to the functionality f.

4.2.1 Percentage of penetrated monomers

The first approach for the estimation of the core region of the stars is based on calculating the radial distribution function. Radial distribution function, g_{inter} shows the probability of finding external units (units which do not belong to the given star) in a distance d from the central C atom of the chosen star.

For the above calculation we divide the space around the star into radial layers of width Δd centered in the central atom of the kernel. In each layer the total number of units is $M_{\text{all}} = M_{\text{ext}} + M_{\text{st}}$, where M_{ext} is the number of monomers of different stars of the systems and M_{st} the number of monomers belonging to the given star. We calculate the number of monomers of different stars of the systems (M_{ext}) in each layer as it is shown in Fig. 4.14. For the calculation of $g_{\text{inter}}(d)$ we use the equation below:

$$g_{\text{inter}}(d) = \frac{M_{\text{ext}}[d, d+\Delta d]}{\Delta V[d, d+\Delta d] \int_0^{\frac{L}{2}} g_{\text{all}}(d)\ \mathrm{d}d} \tag{4.16}$$

where $g_{\text{all}}(d) = \frac{M_{\text{all}}[d,d+\Delta d]}{\Delta V[d,d+\Delta d]}$ and we divide $g_{\text{inter}}(d)$ by the quantity $\int_0^{\frac{L}{2}} g_{\text{all}}(d)\ \mathrm{d}d$ in order to normalize it in this way.

We average this number over the total number of the monomers in all the shells and over the whole trajectory. The plotted data of radial distribution function, g_{inter}, of $(\text{PS})_f$ and $(\text{PS})_{f/61}$ melt systems are presented in Fig. 4.15.

As expected, there is a region close to the central atom of the dendritic structure (kernel) where the number of external monomers is very small. The radius of this region differs with respect to the star functionality. For functionalities $f = 16$ and $f = 32$ there is a substantial range of d wherein almost no

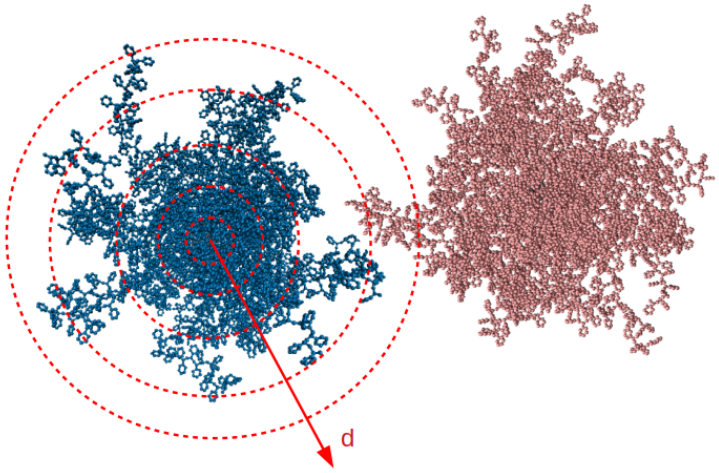

Figure 4.14: Snapshots of two randomly selected stars and the defined radial layers. d is the mean distance between the layer and the central C atom of the star. For the calculation of radial distribution function g_{inter}, only the monomers belonging to the red star have been consider.

external monomers (g_{inter} approximately zero) are found. Examination of this range could be used as the first approximation for the radius of the impenetrable region of the star (d_c). For functionalities $f = 4$ and $f = 8$, at distances $d \approx 0$, g_{inter} is non zero.

From the cumulative sum of g_{inter} we are able to export quantitative information about the radius of the impenetrable region of the star. A cumulative sum is a sequence of partial sums of a given sequence. Which means that by calculating the cumulative sum of g_{inter} in distance $d = R_{g_{mol}}$, we get the percentage of penetrated monomers in the whole region of $d \leq R_{g_{mol}}$. This happens because of the way we have normalized the quantity under investigation, which means that the 100% correspond to the sum of external (i.e., intermolecular monomers) and internal monomers (M_{all}). In Fig. 4.16 we plot the data for the percentage of penetrated monomers in $d \leq R_{g_{mol}}$ as a function of functionality f. For $f = 4$ the percentage of penetrated monomers appears to be significantly larger than for those of higher functionalities. The percentage of penetrated monomers at higher functionalities ($f \geq 16$) appears to be less than 10% of the total number of monomers (internal and external). For $f = 32$ only 5% of the monomer are penetrated which is an evidence for the soft colloidal behavior. Due to the non-monotonic character of the quantity and the sudden

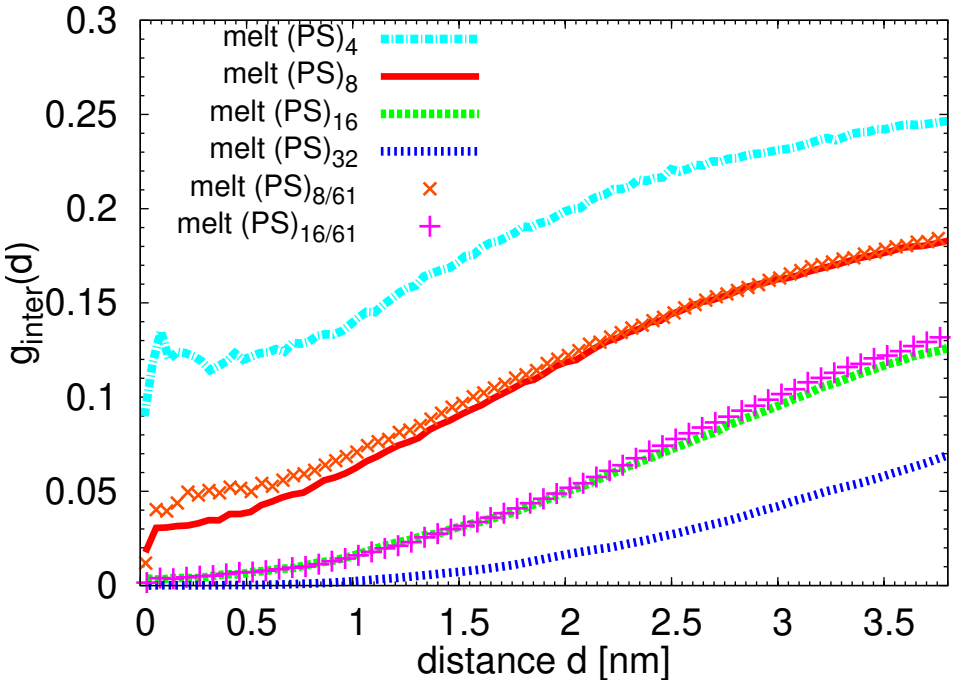

Figure 4.15: Radial probability distribution function of the external atoms (atoms which do not belong in the certain star) for melt systems $(PS)_f$ and for melts of stars with modified kernel $(PS)_f/61$.

drop at $f = 8$ we can assume that for $f > 8$ the stars are not easily penetrable.

We also use the cumulative sum to obtain information about the distance d from the central C atom of the star, at which only a very small number of penetrated monomers can be found. In order to do so, we define the very small amount of external monomers as 1% of the penetrated monomers in g_{inter}. Then, the distance which corresponds to the 1% of the penetrated monomers will be a good estimation of the radius of the core region, d_c. We divide the data by $R_{g_{mol}}$ so that they can be comparable to each other and in Fig. 4.17 we present the core fraction (see eq 4.15) as a function of functionality f. We can see that the core fraction increases with increasing functionality and shows a change in the tendency for $f = 16$. We also examined the same quantity that corresponds to 5% of the penetrated monomers and we observed the same tendency. Our data for the estimation of the radius of the impenetrable region (d_c) are in the range of values obtained from the experimental work on similar systems [11]. The trends reported in this work are in agreement with our data, however, one has to keep in mind that the assumptions used in that work such as Zimm-Stockmayer eq. 4.5 are not valid in our systems. In Chap. 4.1.2 (see Fig. 4.3) we showed that our detailed atomistic predictions do not follow Zimm-Stockmayer

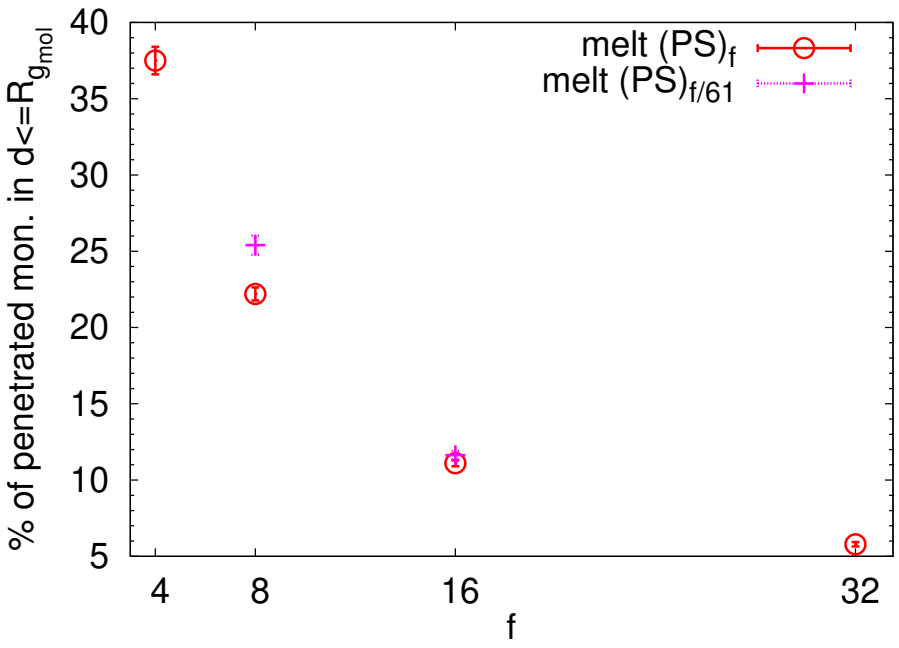

Figure 4.16: Percentage of penetrated monomers within a volume corresponding to the radius of gyration of the star with respect to its functionality f.

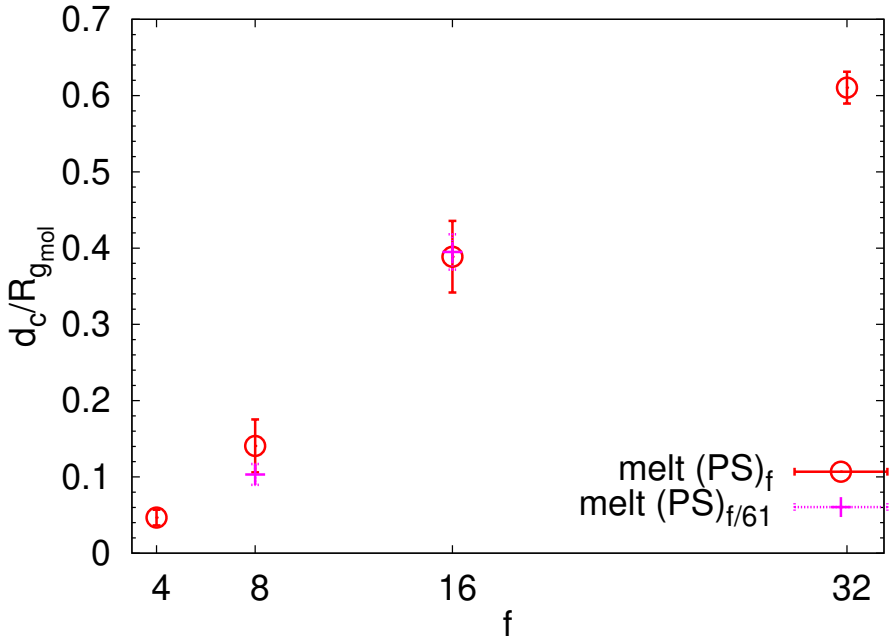

Figure 4.17: The radius of the region around the central C atom where only 1% of the external monomers is present, normalized by $R_{g_{mol}}$ and showed as a function functionality.

prediction, so $R_{g_{mol}}$ cannot be approximated by this model.

4.2.2 Void spaces

For the purpose of the core estimation we study the void spaces of the system. This quantity could give us additional information about packing of the monomers in the system. The coordinates of every atom of the system correspond to its center of mass but in reality the atoms are not point particles. In order to estimate the free space around them we have to take into account their diameter σ. The diameters of each type of united atom are given by the force field and are summarized in Tab. 4.3.

United atom	σ **[nm]**
C (kernel)	0.6400
CH1	0.4650
CH2	0.3950
CH3	0.3750
C (aromatic ring)	0.3700
CH (aromatic ring)	0.3695

Table 4.3: Diameters of atomic units.

For the calculation of the free space we describe a geometrical algorithm, similar to the one reported in [37]. Namely:

Step 1:
We divide the volume of the simulation box into a cubic grid with spacing s. As grid points M_{total} we define the crosspoints of the grid. The grid space ranges from s=0.05nm to s=0.5nm. The upper limit would correspond approximately to the biggest value of σ.

Step 2:
We expand all the atomic units within their corresponding atomic radii ($\frac{\sigma}{2}$) given in Tab. 4.3.

Step 3:
We define the occupation of each point of the grid. Every grid point that is further than the corresponding distance $\frac{\sigma}{2}$ from any atom of the box is defined as a free point. Since σ stands for the diameter of each atom this means that a free point is the one that does not overlap by any atom of the system. We

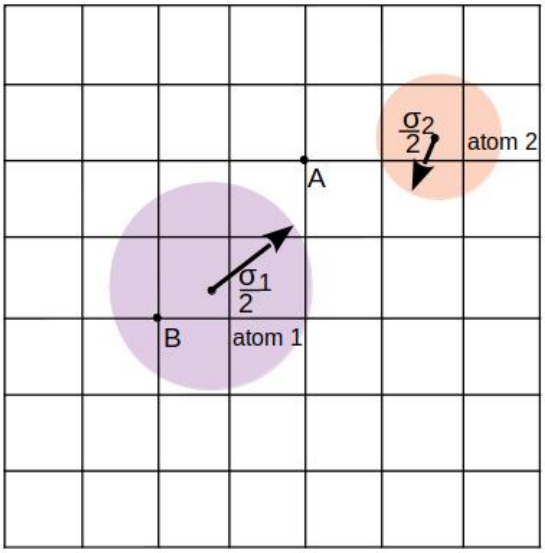

Figure 4.18: Schematic (2D) representation of the procedure of defining grid points as free. Assuming that the two red spheres are two united atoms and σ_1 and σ_2 their atomic diameters, correspondingly. The grid point A is defined as free as its distance from the centers of both atoms 1 and 2 is larger than $\frac{\sigma_1}{2}$ and $\frac{\sigma_2}{2}$, respectively. The grid point B is not defined as free because its distance from atom 1 is smaller than $\frac{\sigma_1}{2}$.

count the total number of the free points of the grid (M_{free}) and store their coordinates.

Step 4:
We calculate the free volume fraction Φ which equals to:

$$\Phi = \frac{M_{free}}{M_{total}}. \tag{4.17}$$

The whole process of defining one grid point as free is described schematically in Fig. 4.18. Also, in Fig. 4.19 we present a snapshot of a randomly selected melt system, where every star is highlighted by a different color and the same snapshot with the defined grid of randomly selected length s.

In order to improve the accuracy of our calculations we analyze this quantity for several (here 9) frames -randomly selected but uniformly distributed over the trajectory- instead of the whole trajectory. The final value of Φ and corresponding error bars (for $s = 0.1$, see below) are given by averaging the values of each one of the selected frames and estimating the standard deviation.

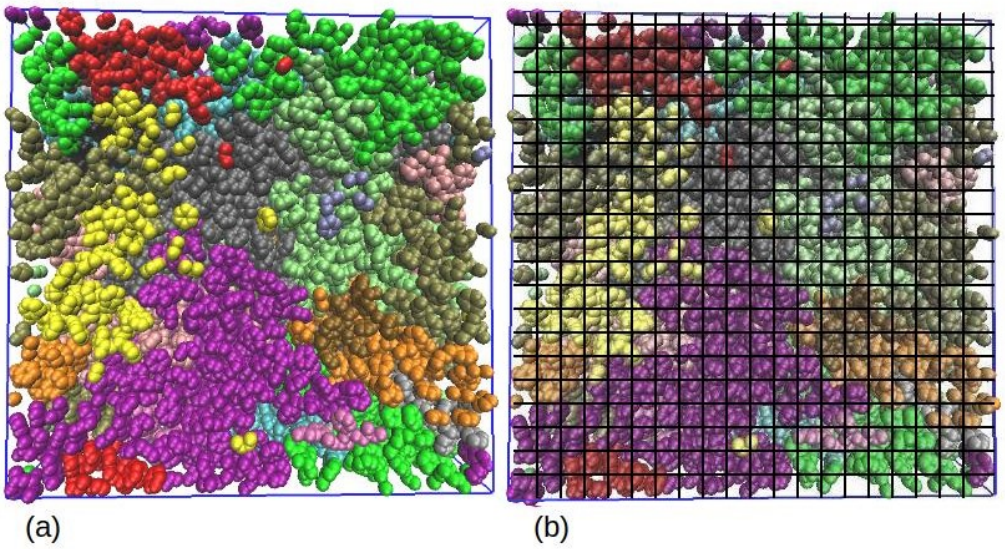

Figure 4.19: (a) Snapshot of a randomly selected melt system $(PS)_8$ inside the periodic simulation box (blue square). Every star is defined by a different color. The radius of the atoms does not correspond to the exact radius given by the force field. (b) The same snapshot of $(PS)_8$ with the schematic representation of a grid with randomly selected length s.

For the purpose of an efficient choice of the value of the grid length, we examine the behavior of the fraction Φ with respect to s. In Fig. 4.20 we present the graph of free volume fraction Φ with respect to the grid space s for three selected systems: $(PS)_8$, $(PS)_{32}$ and $(PS)_{8/61}$. In all the systems a short plateau appears for small values of s. Having in mind the efficiency of the code and physical meaning of the grid size, we chose grid space $s = 0.1$ nm, which is smaller than the smallest radius of the atomic units but computationally still accessible.

In Fig. 4.21 we present a comparison of the free volume fraction Φ for systems with different functionalities f and different internal structure with the corresponding error bars. For stars in melt $(PS)_f$ as the functionality increases the free volume fraction decreases. The higher the functionality the less percentage of the free space. Systems with modified kernel (dendritic structure) $(PS)_{f/61}$ do not seem to be affected by the change of the functionality and both stars with $f = 8$ and $f = 16$ exhibit very similar values of Φ. However, they seem to slightly differ from those with the same functionality but unmodified kernel, $(PS)_f$. Systems with stars of $f = 8$ with ″bigger″ kernel ($(PS)_{8/61}$) seem to have less free space than the one with the ″smaller″ one $(PS)_8$. The opposite trend is observed for the pair of stars with $f = 16$, more specifically the value

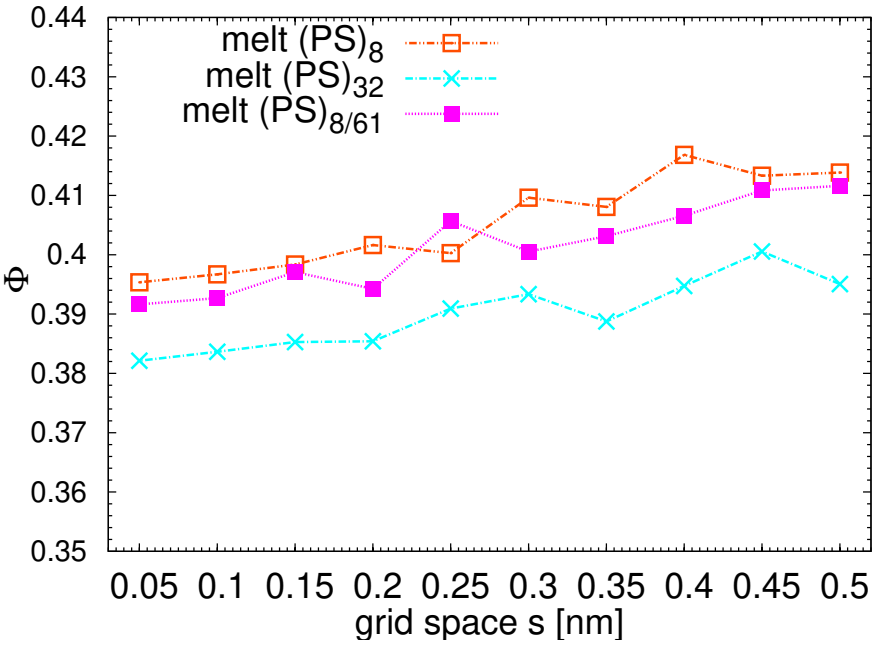

Figure 4.20: Free volume fraction Φ as a function of grid length s for melt $(PS)_8$ (empty squares), $(PS)_{8/61}$ (full squares) and $(PS)_{32}$ (crosses) systems.

of free volume fraction is higher for $(PS)_{16/61}$ that for $(PS)_{16}$.

For a better analysis of the void space around the star we calculate the distance of every free point from the center of each star. In Fig. 4.22 we present the radial distribution $g_{\text{void}}(d)$ of these distances for chosen grid space $s = 0.1$ nm, for every melt system under investigation. For a better comparison we divide the distances d by the radius of gyration $R_{g_{mol}}$ of the corresponding system. We have normalized the distribution in a way that the area (integral) below the curve equals to 1.

In the way we plotted the data $(d/R_{g_{mol}})$ we can easily observe that in $d = R_{g_{mol}}$ (point 1 on x-axis) and in a region around this point the distribution reaches a plateau. In addition, for systems consisting of stars of $f = 16, 32$ the plateau seems to be reached at $d = d_c$ (see Fig. 4.17). For $d \geq d_c$, the distributions for the stars with $f = 16$ (melt $(PS)_{16}$ and melt $(PS)_{16/61}$) overlap.

For smaller distances $(d < d_c)$ we do not observe any overlaps of the data of different systems. Moreover, for $(PS)_{f/61}$ stars the region close to the center of the star wherein there are no free points is wider than the corresponding region for stars with non-modified kernel $(PS)_f$.

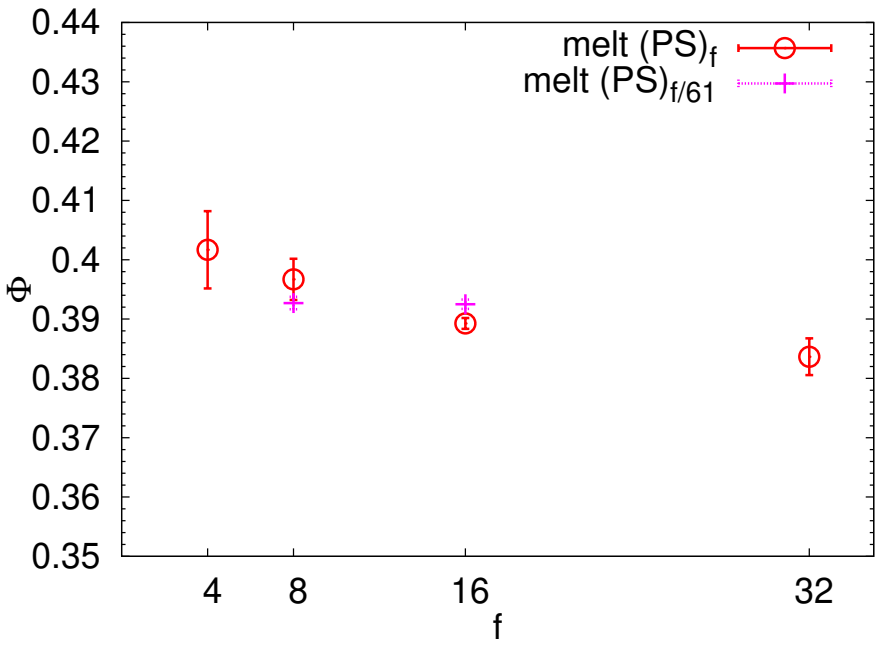

Figure 4.21: Free volume fraction as a function of functionality f for stars in melt with the corresponding error bars. The grid size is 0.1 nm.

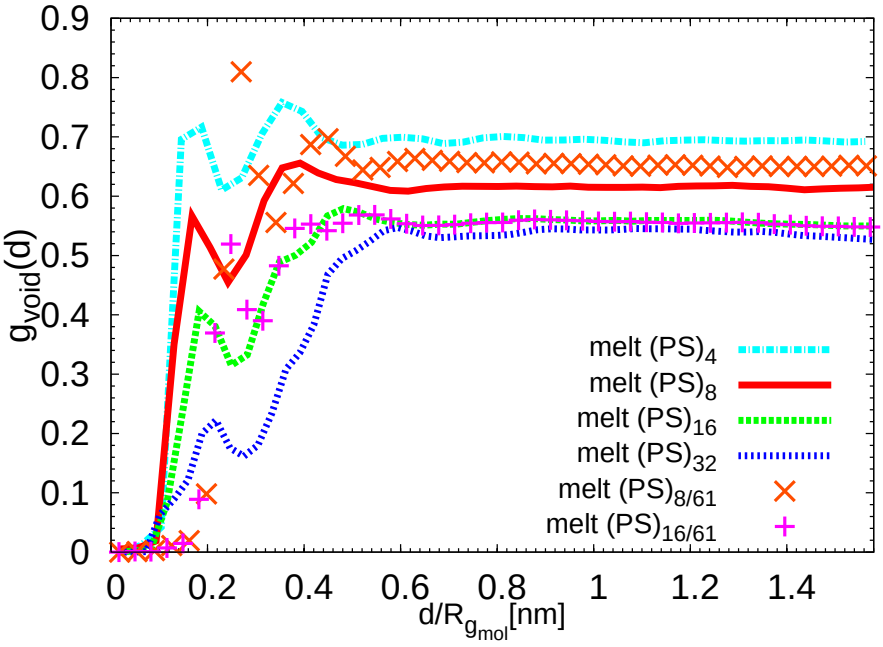

Figure 4.22: Radial distribution of the distances between the free points of the grid and the centers of the kernel of the stars for the systems of melt $(\mathrm{PS})_f$ (lines) and stars $(\mathrm{PS})_{f/61}$ (symbols) with the modified dendritic structure.

5. Conclusions

The aim of this thesis was to study the structural behavior of polystyrene (PS) star-shaped polymers in melts. To our knowledge, it is the first time that star-like polymers in melt are studied by a detailed atomistic model.

In order to achieve our goal, we performed atomistic MD simulations of polystyrene (PS) star-shaped polymers of functionalities (number of arms) f=4, 8, 16, 32 in melts. For a better comparison of the results we also prepared models of PS star-shaped polymers in blends with linear PS chains and some with modified internal structure. After the performance of equilibration runs, the systems do not exhibit any deformations and we were able to calculate a variety of statistical quantities for the structural analysis of the materials. The results are presented as functions of f and comparisons between our data, theory and experimental data have been made.

The size of the stars in the melt does not deviate from the corresponding ones in blends and seems to follow a power law similar to the one suggested by Grest [35]. Consequently, our results do not agree with the theoretical prediction of Zimm-Stockmayer (see Fig. 4.3) [34].

The shape of the stars is strongly affected by the functionality. With increasing functionality the stars get more spherical. In blends the stars are slightly more spherical than those with the same functionality in melts. The modification of the star kernel does not affect the shape parameters.

The density profile along the star arms for each system is non-monotonic as it was expected from the theoretical models. In every star there is a region around its center where the density is higher than the mean density of the system. The radius of this region increases in a proportion to the functionality. The effect of the modification of the star kernel is apparent in the density profile of the star with $f = 8$, which deviates from the one of the corresponding star with unmodified kernel and approximates more the profile observed for the star with $f = 4$.

Concerning the positions of the center-of-mass of the stars, we showed that for $f \leq 8$ there are stars which can be in a distance smaller than their radius of gyration $R_{g_{mol}}$. Stars with $f = 4$ have a prolate shape what helps them to

align next to each other. For $f > 8$ we did not detect distances smaller than $R_{g_{mol}}$ and thus these stars are not easily penetrable.

For the estimation of the impenetrable region of the stars (core with radius d_c) we used various methods. We found out that the percentage of penetrated monomers in a region smaller than $R_{g_{mol}}$ decreases with functionality and shows a change in the tendency for $f = 16$. The same trend was observed for the ratio $d_c/R_{g_{mol}}$ estimated in a similar way. This trend is in agreement with experimental study on similar systems [11]. We performed an estimation of the free volume in the systems based on geometrical assumptions, where a grid was applied to divide each simulation box. As anticipated, we found less free space in the systems of stars with higher functionality. The distributions of the free points around the center of the star depend on the size of the kernel.

In summary, we showed that atomistic simulations are very powerful tool to quantify structural properties of star-like polymers in melt and that the results can be used to test theoretical predictions and to gain more insight into experimental tendencies.

The complexity of such systems gives us the opportunity to study a wide range of properties. The analysis of void space in the systems is open to further investigation such as a cluster analysis of the free points. The dynamical properties of PS star-shaped polymers will be also studied in future work, which will provide us information about important industrial properties and their dependence on the functionality of the star.

6. Appendix

TRAPPE

Atom types

Atomic Unit	mass	charge	p type	σ [nm]	ϵ [kJoule /mol]
C	12.0110	0.0000	A	0.6400	0.004157
CH1	13.0190	0.0000	A	0.4650	0.0831
CH2	14.0270	0.0000	A	0.3950	0.3828
CH3	15.0350	0.0000	A	0.3750	0.8159
Car	12.0110	0.0000	A	0.3700	0.2494
CHar	13.0190	0.0000	A	0.3695	0.4197

Bond types

Atomic unit i	Atomic unit j	func	b0 [nm]	kb[kJ/ mol*nm^2]
CH2	CH2	1	0.154000	217700.00
CH3	CH1	1	0.154000	200000.00
CH1	Car	1	0.151000	200000.00
Car	CHar	1	0.140000	400000.00
CHar	CHar	1	0.140000	400000.00
CH1	CH2	1	0.154000	200000.00
C	CH1	1	0.154000	217700.00
CH1	CH1	1	0.154000	217700.00

Angle types

Atomic unit i	Atomic unit j	Atomic unit k	func	θ_0 [deg]	cth [kJ/ mol*rad^2]
CH3	CH1	CH2	1	112.00	520.00
CH3	CH1	Car	1	112.00	520.00
Car	CH1	CH2	1	112.00	520.00
CH1	CH2	CH1	1	114.00	520.00
CHar	Car	CH1	1	120.00	1000.00
CHar	Car	CHar	1	120.00	1000.00
CHar	CHar	Car	1	120.00	1000.00
CHar	CHar	CHar	1	120.00	1000.00
CH2	CH1	CH2	1	112.00	520.00
CH1	C	CH1	1	109.50	520.00
C	CH1	CH2	1	112.0	520.00
CH1	CH1	CH2	1	112.0	520.00
CH1	CH1	CH1	1	112.0	520.00
CH1	CH2	CH2	1	114.0	520.00

Table 6.1: TRAPPE of PS star-shaped homopolymer

Dihedral types					
Atomic unit i	**Atomic unit j**	**Atomic unit k**	**Atomic unit l**	**func**	**C_n prefactors [kJ/mol]**
CH3	CH1	CH2	CH1	3	C_0:8.3974, C_1:16.7862 C_2:1.1340, C_3:-26.3160 C_4:0.0000, C_5:0.0000
CH1	CH2	CH1	CH2	3	C_0:8.3974, C_1:16.7862 C_2:1.1340,C_3:-26.3160 C_4:0.0000, C_5:0.0000
CHar	Car	CH1	CH2	1	C_0:240.00, C_1:1.3889 C_2:2
CHar	Car	CH1	CH3	1	C_0:240.00, C_1:1.3889 C_2:2
Car	CHar	CHar	CHar	2	C_0:0.0000, C_1:167.3600
CHar	CHar	CHar	CHar	2	C_0:0.0000, C_1:167.3600
CHar	CHar	Car	CHar	2	C_0:0.0000, C_1:167.3600
Car	CHar	CHar	CH1	2	C_0:0.0000, C_1:167.3600
CH1	CH2	CH3	Car	2	C_0:35.2600, C_1:334.8000
CH1	CH3	CH2	Car	2	C_0:35.2600, C_1:334.8000
CH1	CH2	CH2	Car	2	C_0:35.2600, C_1:334.8000
CH2	CH1	CH2	CH2	3	C_0:8.3974, C_1:16.7862 C_2:21.1340, C_3:-26.3160 C_4:0.0000, C_5:0.0000
CH2	CH2	CH1	CH1	3	C_0:8.3974, C_1:16.7862 C_2:1.1340, C_3:-26.3160 C_4:0.0000, C_5:0.0000
CH1	CH1	CH1	CH2	3	C_0:8.3974, C_1:16.7862 C_2:1.1340, C_3:-26.3160 C_4:0.0000, C_5:0.0000
CH1	CH2	CH2	CH2	3	C_0:8.3974, C_1:16.7862 C_2:1.1340, C_3:-26.3160 C_4:0.0000, C_5:0.0000
CH1	CH2	CH2	CH1	3	C_0:8.3974, C_1:16.7862 C_2:1.1340, C_3:-26.3160 C_4:0.0000, C_5:0.0000
C	CH1	CH2	CH2	3	C_0:8.3974, C_1:16.7862 C_2:1.1340 , C_3:-26.3160 C_4:0.0000, C_5:0.0000
CH1	C	CH1	CH2	3	C_0:8.3974, C_1:16.7862 C_2:1.1340 , C_3:-26.3160 C_4: 0.0000, C_5:0.0000
CH1	CH1	CH1	CH1	3	C_0:8.3974, C_1:16.7862 C_2:1.1340, C_3:-26.3160 C_4: 0.0000, C_5:0.0000

Table 6.2: (continue) TRAPPE of PS star-shaped homopolymer

Bibliography

[1] D. I. Bower, *An Introduction to Polymer Physics*. Cambridge, 2002.

[2] M. Rubinstein and R. Colby, *Polymer Physics*. Oxford University Press, 2003.

[3] R. H. Petrucci, W. Harwood, and F. Geoffrey Herring, *General Chemistry : Principles and Modern Applications / R.H. Petrucci, W.S. Harwood, F.G. Herring.* 01 2002.

[4] D. Vlassopoulos, G. Fytas, T. Pakula, and J. Roovers, "Multiarm star polymers dynamics," *Journal of Physics: Condensed Matter*, vol. 13, 09 2001.

[5] E. Glynos, L. Papoutsakis, W. Pan, E. P. Giannelis, A. D. Nega, E. Mygiakis, G. Sakellariou, and S. H. Anastasiadis, "Nanostructured polymer particles as additives for high conductivity, high modulus solid polymer electrolytes," *Macromolecules*, vol. 50, no. 12, pp. 4699–4706, 2017.

[6] E. Glynos, P. Petropoulou, E. Mygiakis, A. D. Nega, W. Pan, L. Papoutsakis, E. P. Giannelis, G. Sakellariou, and S. H. Anastasiadis, "Leveraging molecular architecture to design new, all-polymer solid electrolytes with simultaneous enhancement in modulus and ionic conductivity," *Macromolecules*, vol. 51, no. 7, pp. 2542–2550, 2018.

[7] D. Vlassopoulos, "Colloidal star polymers: Models for studying dynamically arrested states in soft matter," *Journal of Polymer Science Part B: Polymer Physics*, vol. 42, pp. 2931 – 2941, 08 2004.

[8] S. Coppola, N. Grizzuti, G. Floudas, and D. Vlassopoulos, "Viscoelasticity and crystallization of poly(ethylene oxide) star polymers of varying arm number and size," *Journal of Rheology - J RHEOL*, vol. 51, 09 2007.

[9] L. B. S. R. E. van Ruymbeke, S. Coppola and D. Vlassopoulos, "Decoding the viscoelastic response of polydisperse star/linear polymer blends," *Journal of Rheology - J RHEOL*, vol. 47, pp. 507–538, 2010.

[10] Daoud, M. and Cotton, J.P., "Star shaped polymers : a model for the conformation and its concentration dependence," *J. Phys. France*, vol. 43, no. 3, pp. 531–538, 1982.

[11] K. J. Johnson, E. Glynos, G. Sakellariou, and P. Green, "Dynamics of star-shaped polystyrene molecules: From arm retraction to cooperativity," *Macromolecules*, vol. 49, no. 15, pp. 5669–5676, 2016.

[12] T. Pakula, "Static and dynamic properties of computer simulated melts of multiarm polymer stars," *Computational and Theoretical Polymer Science*, vol. 8, no. 1, pp. 21 – 30, 1998.

[13] "Polystyrene." http://www.chemicalsafetyfacts.org/polystyrene.

[14] D. Frenkel and B. Smit, eds., *Understanding Molecular Simulation: From Algorithms to Applications*. Orlando, FL, USA: Academic Press, Inc., 1st ed., 1996.

[15] M. Allen, M. Allen, D. Tildesley, T. ALLEN, and D. Tildesley, *Computer Simulation of Liquids*. Oxford Science Publ, Clarendon Press, 1989.

[16] E. Winsberg, "Computer simulations in science." http://plato.stanford.edu/archives/spr2019/entries/simulations-science/, 2019.

[17] P. Holmes, "Poincaré, celestial mechanics, dynamical-systems theory and "chaos"," *Physics Reports*, vol. 193, no. 3, pp. 137 – 163, 1990.

[18] K. Johnston and V. Harmandaris, "Hierarchical simulations of hybrid polymer–solid materials," *Soft Matter*, pp. 6696–6710, 2013.

[19] "Introduction to parallel computing." http://computing.llnl.gov/tutorials/.

[20] P. Bačová, R. Foskinis, E. Glynos, A. N. Rissanou, S. H. Anastasiadis, and V. Harmandaris, "Effect of macromolecular architecture on the self-assembly behavior of copolymers in a selective polymer host," *Soft Matter*, vol. 14, pp. 9562–9570, 2018.

[21] P. Bačová, E. Glynos, S. H. Anastasiadis, and V. Harmandaris, "Nanostructuring single-molecule polymeric nanoparticles via macromolecular architecture," *ACS Nano*, vol. 13, no. 2, pp. 2439–2449, 2019.

[22] F. Snijkers, H. Y. Cho, A. Nese, K. Matyjaszewski, W. Pyckhout-Hintzen, and D. Vlassopoulos, "Effects of core microstructure on structure and dynamics of star polymer melts: From polymeric to colloidal response," *Macromolecules*, vol. 47, no. 15, pp. 5347–5356, 2014.

[23] W. F. V. Gunsteren and H. J. C. Berendsen, "A leap-frog algorithm for stochastic dynamics," *Molecular Simulation*, vol. 1, no. 3, pp. 173–185, 1988.

[24] V. A. Harmandaris, K. C. Daoulas, and V. G. Mavrantzas, "Molecular dynamics simulation of a polymer melt/solid interface: local dynamics and chain mobility in a thin film of polyethylene melt adsorbed on graphite," *Macromolecules*, vol. 38, no. 13, pp. 5796–5809, 2005.

[25] S. Nosé, "A molecular dynamics method for simulations in the canonical ensemble," *Molecular Physics*, vol. 52, no. 2, pp. 255–268, 1984.

[26] H. Berendsen, J. van Postma, W. van Gunsteren, A. DiNola, and J. Haak, "Molecular-dynamics with coupling to an external bath," *The Journal of Chemical Physics*, vol. 81, p. 3684, 10 1984.

[27] E. L. B. H. M.J. Abraham, D. van der Spoel and the GROMACS development team, "Gromacs user manual version 2019,"

[28] "Viscoelasticity and molecular rheology," in *Polymer Science: A Comprehensive Reference* (K. Matyjaszewski and M. Möller, eds.), pp. 133 – 179, Amsterdam: Elsevier, 2012.

[29] C. D. Wick, M. G. Martin, and J. I. Siepmann, "Transferable potentials for phase equilibria. 4. united-atom description of linear and branched alkenes and alkylbenzenes," *The Journal of Physical Chemistry B*, vol. 104, no. 33, pp. 8008–8016, 2000.

[30] R. Auhl, R. Everaers, G. S. Grest, K. Kremer, and S. J. Plimpton, "Equilibration of long chain polymer melts in computer simulations," *The Journal of Chemical Physics*, vol. 119, no. 24, pp. 12718–12728, 2003.

[31] P. Bačová, L. G. D. Hawke, D. J. Read, and A. J. Moreno, "Dynamics of branched polymers: A combined study by molecular dynamics simulations and tube theory," *Macromolecules*, vol. 46, no. 11, pp. 4633–4650, 2013.

[32] C. Likos, "Effective interactions in soft condensed matter physics," *Physics Reports-review Section of Physics Letters - PHYS REP-REV SECT PHYS LETT*, vol. 348, pp. 267–439, 07 2001.

[33] J. E. Mark, *Physical Properties of Polymer Handbook*, vol. 29. 01 2007.

[34] B. H. Zimm and W. H. Stockmayer, "The dimensions of chain molecules containing branches and rings," *The Journal of Chemical Physics*, vol. 17, no. 12, pp. 1301–1314, 1949.

[35] G. S. Grest, L. J. Fetters, J. S. Huang, and D. Richter, *Star Polymers: Experiment, Theory, and Simulation*, pp. 67–163. John Wiley and Sons, Ltd.

[36] "Error analysis in experimental physical science." https://faraday.physics.utoronto.ca/PVB/Harrison/ErrorAnalysis/Propagation.html.

[37] H. J. Butt, H. Duran, W. Egger, F. Faupel, V. Harmandaris, S. Harms, K. Johnston, K. Kremer, F. Y. Lin, L. Lue, C. Ohrt, K. Raetzke, L. Ravelli, W. Steffen, and S. D. B. Vianna, "Interphase of a polymer at a solid interface," *Macromolecules*, vol. 47, no. 23, pp. 8459–8465, 2014.